The Planetary Science Journal, 6:41 (31pp), 2025 February https://doi.org/10.3847/PSJ/ada7ef

Informed Design of a Gravity Science Experiment for the Future Geophysical Investigation of the Uranian Moons

Valerio Filice[1,2], Gael Cascioli[3,4], Sébastien Le Maistre[1,2], Rose-Marie Baland[2], Antony Trinh[2], Erwan Mazarico[4], and Sander Goossens[4]

[1] Earth and Life Institute, Université catholique de Louvain, Place Louis Pasteur 3, 1348 Louvain-la-Neuve, Belgium
[2] Reference Systems and Planetology, Royal Observatory of Belgium, 3 Avenue Circulaire, 1180 Uccle, Belgium
[3] University of Maryland Baltimore County, 1000 Hilltop Circle, Baltimore, MD 21250, USA
[4] Planetary Geology, Geophysics, and Geochemistry Laboratory, NASA Goddard Space Flight Center, 8800 Greenbelt Road, Greenbelt, MD 20771, USA
Received 2024 August 1; revised 2024 December 13; accepted 2024 December 14; published 2025 February 7

Abstract

The outer solar system beyond Saturn remains unexplored by dedicated orbital missions. With a launch window opening in 2029, the Uranus Orbiter and Probe (UOP) mission has been prioritized as a NASA Flagship mission for the next decade (2023–2032) to comprehensively study Uranus and its major moons—Miranda, Ariel, Umbriel, Titania, and Oberon. We define and apply novel mission design principles centered on scientific objectives to UOP's gravity science (GS) experiment. Using a combination of Bayesian and Precise Orbit Determination inversions, it is possible to determine mission requirements ensuring the achievement of scientific goals. Our methodology involves building measurement-to-interior parameter maps via extensive Markov Chain Monte Carlo simulations, linking geodetic measurements' precisions to uncertainties in key interior parameters of the Uranian moons. We show how this mapping approach allows for the rapid evaluation of the ability of a GS experiment design to constrain interior parameters. We conduct a covariance analysis of two orbital tours, multiple measurement strategies, and inversion settings. The tested cases enable the satisfactory determination of Ariel's ice shell thickness (to about 16%), as well as its rock-to-ice mass ratio (≈28%). None of the solutions were able to constrain its ocean thickness. This reverse approach allows for the rapid and scientifically informed adjustment of mission design, thereby demonstrating its potential applicability to other planetary science experiments.

Unified Astronomy Thesaurus concepts: Remote sensing (2191); Deep space probes (366); Uranian satellites (1750); Planetary interior (1248); Markov chain Monte Carlo (1889); Gravitational fields (667); Tides (1702); Libration (917)

Materials only available in the online version of record: figure sets, machine-readable table

1. Introduction

So far, the outer solar system beyond Saturn has never been explored with a dedicated orbital mission. Our current knowledge of Uranus and its major moons, Miranda, Ariel, Umbriel, Titania, and Oberon, mostly comes from Earth-based observations (e.g., R. Cartwright et al. 2015) and in situ measurements from the Voyager 2 spacecraft, which flew by the Uranian system in 1986 January (B. A. Smith et al. 1986; G. L. Tyler et al. 1986). A 10 yr launch window to Uranus will open in 2029, prompting the scientific community to prioritize a mission to the Uranian system. Consequently, the Planetary Science and Astrobiology Decadal Survey selected the Uranus Orbiter and Probe (UOP) mission concept (A. Simon et al. 2021) as the highest-priority new NASA Flagship mission for the decade 2023–2032 (National Academies of Sciences 2023).

The UOP mission aims to conduct a comprehensive and interdisciplinary study of the Uranian system, exploring its origins, processes, and habitability. In addition to addressing specific science questions about the enigmatic ice giant Uranus, UOP would place particular emphasis on exploring the major satellites of Uranus. While Voyager 2 and Earth-based observations have provided partial insights into these bodies, the lack of a dedicated mission has left many fundamental questions unanswered. Of particular importance, given the newly discovered astrobiological potential of other icy moons, is the question whether any of the Uranian satellites have or have had habitable conditions. A primary scientific objective entails the constraining of the interior composition of these satellites.

The notional payload of the UOP spacecraft includes a comprehensive suite of instruments, notably a 3.1 m high-gain antenna (HGA) and an ultrastable oscillator, to enable a gravity science (GS) experiment. Additionally, the payload includes a narrow-angle camera (NAC) and a wide angle camera (WAC), whose objective is to characterize the global shape of the moons and to determine the distribution and topography of surface features (A. Simon et al. 2021).

Radiometric and optical measurements have proven very effective in determining the internal structure and rock-to-ice mass ratio, as well as in detecting liquid layers inside icy satellites. For example, Doppler tracking data collected by the Radio Science Subsystem experiment of the Cassini mission revealed the presence of a global ocean beneath the surface of Titan (L. Iess et al. 2012; D. Durante et al. 2019; S. Goossens et al. 2024), also supported by the large obliquity estimated from synthetic aperture radar images acquired by the Cassini RADAR experiment (B. W. Stiles et al. 2008; B. G. Bills & F. Nimmo 2009; R. M. Baland et al. 2011; R. Meriggiola et al. 2016). In parallel, landmark tracking data acquired by the

Cassini Imaging Science Subsystem have allowed the estimation of the diurnal libration amplitude of Mimas and Enceladus, also revealing the presence of global subsurface oceans in these worlds (R. Tajeddine et al. 2014; I. E. Nadezhdina et al. 2016; P. Thomas et al. 2016; R. S. Park et al. 2024).

Despite their wide use for inference of geophysical properties, remote-sensing GS experiments do not provide direct and explicit information about the interior structure of a body, and advanced methods and tools must be developed to retrieve it. Bayesian inference using the Markov Chain Monte Carlo (MCMC) approach represents a highly effective technique for addressing complex inverse problems in the field of space geodesy. This method combines the probabilistic framework of Bayesian inference with the computational efficiency of MCMC algorithms to estimate the posterior distributions of model parameters, for a given set of measurements with accompanying uncertainties, thereby providing a comprehensive quantification of uncertainties (see, e.g., C. P. Robert & G. Casella 2004). A number of measurements from previous missions have been analyzed using MCMC in order to constrain interior structures (e.g., I. Matsuyama et al. 2016 for the Moon, S. Bertone et al. 2021 for Mercury, or S. Goossens et al. 2024 for Titan). MCMC is also increasingly used in mission design, in particular to establish a link between the needed measurement precision (e.g., noise on radiometric data or resolution of imagery data) and the uncertainty with which geodetic properties (e.g., gravity, rotation, or tides) can be estimated (e.g., A. I. Ermakov et al. 2021; F. Petricca et al. 2023; G. Cascioli et al. 2024; A. Genova et al. 2024).

In this work, we present an alternative approach in which the scientific objectives of the mission serve as the primary driver for its design. Such an approach offers a significant advantage, as it allows mission designers to secure scientific objectives while making the necessary adjustments. We apply this new approach to the GS experiment of the UOP mission, which aims to address the scientific questions raised by the latest Planetary Science and Astrobiology Decadal Survey regarding the Uranian satellites. The design of this mission is in its preliminary stages, where payloads and observation strategies are still being defined. This makes it an excellent test case. In Section 2, we explain our working strategy, which consists of the combination of a reverse approach based on the Bayesian inversion technique and Precise Orbit Determination (POD) inversions, allowing us to derive mission requirements (instrument performance and observation strategy) that ensure the achievement of the scientific objectives. In Section 3, we apply the MCMC approach to build lookup tables for uncertainties in interior parameters (densities, thickness, and rock-to-ice mass ratio) corresponding to given measurement precisions on geodetic parameters (mean moment of inertia (MoI), tidal Love number, obliquity, and diurnal libration amplitude), for a range of interior models for each satellite. Readers can access these lookup tables as machine-readable tables (MRTs; see Appendix C). By interpolating from the lookup tables, any uncertainty on one interior parameter can be mapped to a set of geodetic parameter measurements uncertainties. In what follows, we will use the terms “lookup tables” and “maps” interchangeably. We illustrate how these lookup tables facilitate a rapid assessment of the precision required in geodetic measurements to achieve the desired level of uncertainty for any interior parameter and, consequently, any interior objective. In Section 4, we demonstrate a second use of these maps by evaluating different designs for the UOP GS experiment in terms of their ability to meet the scientific goals of the mission. We perform a covariance analysis of the geodetic parameters by simulating synthetic radiometric and optical data, then use the maps developed in Section 3, and finally propose general guidelines for the future development of the UOP GS experiment. Conclusions are gathered in Section 5.

2. The Mapping Method: Driving Mission Design through Science Objectives

In the conventional framework of a GS experiment, the mission design results in an experiment configuration. A POD simulation is then conducted to predict the expected geodetic measurement uncertainties. Finally, an inverse technique (such as, but not limited to, MCMC) is employed to assess the degree to which these uncertainties can constrain the interior structure of the investigated body. This traditional approach can be limiting, as it strongly depends on the specific experiment design at hand (e.g., spacecraft orbit, instrument performance) and frequently necessitates iterative redesigns to meet scientific objectives, especially when confronted with evolving mission constraints (see, e.g., the Europa Clipper case; D. Bindschadler et al. 2022). In light of these limitations, we adopt a “reverse mapping” approach, scaling up works such as that of A. I. Ermakov et al. (2021). Rather than starting with experiment designs, we focus on the desired scientific outcomes, namely the uncertainty on key interior parameters. We then map these back to the required geodetic measurement precisions, which depend directly on the mission design.

One objective of the UOP GS experiment, as highlighted in the UOP Science Traceability Matrix, is to investigate the interior properties of the Uranian satellites. In particular, the objective is to determine their rock-to-ice mass ratio and identify which moons, if any, are ocean worlds. Here we consider Doppler measurements alone or in combination with image landmark tracking data. Other types of measurements, such as the intensity and direction of the magnetic fields, the global shapes, or the detection of plumes/activity, could also contribute to the science goals (A. Simon et al. 2021) but are outside the scope of this study. As indicated in the introduction, GS experiments carried out in the past on icy moons have demonstrated that it is possible to precisely measure the satellite's static gravity, tidal response, spin axis orientation, and libration amplitudes with multiple spacecraft flybys. These geodetic observations allow the inference of some characteristics of the internal structure of the moons, thereby providing critical insights into their composition, thermal state, and formation.

The hydrostatic components of the quadrupole gravity field coefficients J_2 and C_{22} can be used to infer the body's normalized mean MoI (or I/MR^2). The MoI provides insights into the overall density distribution of a body, indicating the extent of differentiation. When combined with data on the body's overall composition (such as its bulk density deduced from its total mass and volume) and an assumption on the hydrosphere density, the MoI can be used to estimate the rocky core density and radius (see, e.g., L. Iess et al. 2014). The relation between the hydrostatic contribution to the gravity field and the MoI can be written using the Radau–Darwin approximation (RDA) for synchronously rotating moons as

(e.g., T. Van Hoolst et al. 2008)

$$\mathrm{MoI} = \frac{I}{MR^2} = \frac{2}{3}\left(1 - \frac{2}{5}\sqrt{\frac{5}{3\Lambda_{2,0}+1} - 1}\right), \qquad (1)$$

with $\Lambda_{2,0} = 2J_2/5q$ and $q = n^2R^3/GM$, where J_2 is the zonal degree-two gravity coefficient, n is the mean motion, R is the body's mean radius, and GM is the standard gravitational parameter. The body's periodic response to tidal forces arising from Uranus's gravity field is described by the Love number k_2 (A. E. H. Love 1911). In the presence of an ocean, the amplitude of k_2 for an icy satellite is primarily driven by the shell thickness, with a secondary influence from its rigidity and viscosity (J. M. Wahr et al. 2006). The rotational state of the body is also influenced by its interior structure as thoroughly discussed in a companion paper (R.-M. Baland et al. 2025). The obliquity (ε) of bodies locked into a Cassini state is an RDA-independent measurement of their differentiation level, as discussed, for instance, by J.-L. Margot et al. (2012) for Mercury. Similarly, the libration amplitude (g_s) provides k_2-independent constraints on the ice shell thickness and rigidity, as discussed by T. Van Hoolst et al. (2016) for Enceladus. By combining the determinations of g_s and k_2, we can expect to resolve the thickness and rigidity of the ice shell more efficiently than when each observation is used alone (T. Van Hoolst et al. 2013).

The MCMC approach applied in this study is analogous to that defined by G. Cascioli et al. (2024). Differently from them, the interior is constrained based on the assumption that measurements of the aforementioned geodetic observables—namely, mass, MoI (as derived from the degree-two gravity coefficients), k_2 Love number, libration amplitude, and obliquity—have been obtained. Specifically, we estimate the parameters (densities and thicknesses) of a three-layer interior by minimizing the residuals between the synthetic geodetic measurements and the geodetic observables as computed from dedicated models. Our three-layer interiors comprise a core, a global liquid layer, and an outer ice shell, each with homogeneous densities. We use ranges of interior models that are fairly consistent with the ranges defined in H. Hussmann et al. (2006), C. J. Bierson & F. Nimmo (2022), and J. Castillo-Rogez et al. (2023). The dedicated models to calculate the geodetic observables are the propagator matrix technique to calculate the k_2 Love number (R. Sabadini et al. 2016) and the models for a satellite with an ocean of R.-M. Baland & T. Van Hoolst (2010) and R.-M. Baland et al. (2019) to compute the libration amplitude and obliquity of the ice shell (we here neglect the small effect of tides on the rotational response). The MoI is calculated by direct integration of the density profile.

Our objective is to assess the expected uncertainties associated with the interior parameters' estimation, such as the ice shell thickness (d_s), ocean thickness (d_o), and rock-to-ice mass ratio, as a function of the geodetic measurement uncertainties (i.e., the precisions on k_2, g_s, ε, and MoI). Since these uncertainties in interior parameters depend on their own true value, a series of truth models representing diverse interior structures, encompassing both ocean-bearing and oceanless cases, are simulated. To this end, the MCMC setup entailed running 625 simulations per satellite truth model, testing measurement precisions ranging from 100% to 0.01% of the signal levels (i.e., of the predicted amplitude of k_2, g_s, ε, and MoI). The extensive range of truth models allows the construction of a comprehensive "lookup table" for each interior parameter, mapping all possible combinations of geodetic measurement uncertainties to their corresponding uncertainties on interior parameters. Specifically, we define the interior parameter uncertainty as half of the range between the 15.87th and 84.13th percentiles of the posteriori distribution. Each MCMC run is defined by 50 model realizations, or walkers, and the affine-invariant ensemble sampler chain for each walker (i.e., the Markov chain) is set to 100,000. In particular, we use the affine-invariant ensemble sampler implemented in the publicly available emcee Python library (D. Foreman-Mackey et al. 2013). We validated this configuration by simulating independently the cases with the most stringent measurement uncertainties and subsequently tested convergence through standard techniques (e.g., chain autocorrelation time). However, as the number of walkers and the chain length required for convergence vary case by case, in order to populate the "lookup tables," we exclude runs where the simulated true value is not within the 5th–95th percentile range of the resulting probability distribution of the parameter of interest. This ensures that the mapping is correctly done. An additional constraint is defined when when the map is created to determine the geodetic measurement precisions starting from an interior objective in order to reject flat a posteriori distributions whose uncertainty will be noninformative. To this end, we discard solutions where the calculated ratio between the width of the 5th–95th percentile range and the width of the uniform prior distributions of the interior parameter of interest is higher than 60%.

The aforementioned "lookup tables" can be used to determine the required geodetic measurement uncertainties following the definition of an interior-related scientific objective, as detailed in Section 3. They can also be used to quickly assess the performance of an experiment in terms of interior parameters, given the expected uncertainty associated with the geodetic parameters as shown in Section 4. This mapping approach can therefore offer a significant advantage by enabling mission designers to make necessary trade-offs without sacrificing scientific returns. By initially focusing on desired scientific outcomes and mapping these to the required geodetic measurement uncertainties, designers can easily identify which geodetic measurements require high precision and which can tolerate larger uncertainties. Consequently, they can allocate resources more efficiently to ensure that the most crucial geodetic measurements given a scientific objective receive the necessary attention and investment. Furthermore, by establishing a comprehensive relationship between geodetic measurement quality and scientific objectives, we can maintain flexibility in the mission design. As the mission preparation progresses and new constraints emerge, this approach allows for informed adjustments to be made without jeopardizing the scientific goals.

In the following sections, we apply this approach to the five major Uranian satellites in order to provide useful guidelines for the design and implementation of the UOP GS experiment.

3. A Forward Application Framework: Linking Interior Structure to Geodetic Measurement Requirements

The five major Uranian satellites are small to medium sized, with radii ranging from 235.8 km for the innermost Miranda to 788.9 km for the second-to-last Titania (P. C. Thomas 1988;

Table 1
Geodetic Measurement Requirements to Distinguish between Homogeneous and Differentiated Solid Bodies and to Constrain the Hydrosphere Thickness or Detect an Internal Global Ocean from Their Individual Use (Adapted from R.-M. Baland et al. 2025)

Measurement	Goal	Miranda	Ariel	Umbriel	Titania	Oberon
MoI	differentiation			(depends on actual value)		
	hydrosphere thickness	0.005	0.005	0.005	0.005	0.005
Librations	differentiation	5 m	5 m	5 m	0.5 m	0.25 m
	ocean detection*	20 m	5 m	5 m	0.6 m	0.3 m
Obliquity	differentiation	8 m	1 m	2 m	30 m	435 m
	ocean detection			(requires resonance, depends on actual value)		
Love number	differentiation	0.0002	0.0032	0.0032	0.0077	0.0072
	ocean detection (conservative)	0.0002	0.0031	0.0028	0.0067	0.0062
	ocean detection (optimistic)	0.0019	0.0174	0.0165	0.0350	0.0345

Note. MoI requirements correspond to an uncertainty of 50 km on the hydrosphere thickness, except for Miranda (30 km). Libration requirements correspond to the detection of an ocean under an ice shell 150 km thick, except for Miranda (40 km). An asterisk indicates that it requires an independent determination of the MoI at a few percent.

H. Hussmann et al. 2006). Given their relatively small size and mass (R. A. Jacobson 2014), the signature of the static parts of their gravity fields is weak, compared to that of larger icy satellites, like Titan or Europa, which could hinder a precise determination of their MoI. Compared to those of large icy satellites, their periodic tides are also relatively small (k_2 smaller than 0.01 for the Uranian satellites, see R.-M. Baland et al. 2025; vs. 0.4–0.6 for Titan, see L. Iess et al. 2012; D. Durante et al. 2019; S. Goossens et al. 2024). As the amplitude of the rotation signals depends not only on the size of the satellite but also on its orbital parameters, there is a chance of obtaining detectable and useful signals for Uranus's satellites as discussed in R.-M. Baland et al. (2025). For instance, the libration amplitude of Miranda is expected to range between about 40 and 90 m for an ocean thickness between 2.5 and 50 km, against less than 10 m for Ganymede (T. Van Hoolst et al. 2013). Oberon's obliquity could be of the order of $0\overset{\circ}{.}1$, or even larger in the case of a resonance due to the presence of a relatively thin global ocean, values similar to Titan's obliquity ($0\overset{\circ}{.}3$; B. W. Stiles et al. 2008).

On the one hand, the MoI, as an individual measurement, is indicative of the degree of differentiation and, provided that the precision of the measurement is sufficient, of the thickness of the hydrosphere (see J. Castillo-Rogez et al. 2023 for the measurement requirements, revised in R.-M. Baland et al. 2025). A precision of ± 0.005 on the MoI corresponds to no better than 50 km uncertainty on the hydrosphere thickness for all the satellites of Uranus except Miranda, for which it maps to 30 km uncertainty. Excluding homogeneous interiors (MoI = 0.4) is easier, but the required uncertainty depends on the actual value.

On the other hand, the tidal Love number and rotation parameters (diurnal libration amplitude and obliquity), considered separately, could be used to assess differentiation and detect the presence of a global subsurface ocean (R.-M. Baland et al. 2025). The measurement requirements identified in R.-M. Baland et al. (2025) are summarized in Table 1 and commented on here:

1. *Libration requirements.* Confirming the differentiation or presence of an ocean inside Titania and Oberon from a libration measurement would require tighter precision than for the other three satellites. To detect an ocean, an independent estimation of the MoI is needed to help discriminate between possible interiors. As a general rule, the thicker the ocean, the thinner the shell, the larger the libration, and the easier it is to detect the ocean and perhaps even to constrain the thickness of the shell, given the seemingly inverse relation between libration amplitude and shell thickness.
2. *Obliquity requirements.* It would be easier to confirm the differentiation of Miranda, Titania, and Oberon, if they were solid bodies, by measuring obliquity than by measuring libration. The opposite is true for Ariel and Umbriel. In the ocean case, the obliquity is close to that of the solid case, because on the long timescales of precession the body tends to precess as a whole. For some interior structures, however, the presence of the ocean may enhance or reduce the obliquity through resonance between a forcing and a free mode. For Miranda, this may only occur for oceans less than 6 km thick. For the other satellites, a wider range of ocean thicknesses makes resonance possible but not guaranteed.
3. k_2 *requirements.* According to Table 3 in R.-M. Baland et al. (2025), a differentiated body can be distinguished from a homogeneous body with a measurement uncertainty on k_2 of about 0.0002 for Miranda, about 0.0035 for Ariel and Umbriel, and about 0.0075 for Titania and Oberon. These levels of precision also apply to the detection of a liquid ocean, since the lowest value of k_2 in the ocean case for the considered range of interior models is almost equal to the value for the homogeneous case. The aforementioned requirements are approximately 10 times larger for Miranda and approximately 6 times larger for the other satellites, when the upper bounds for k_2 in the ocean case are considered.

The aforementioned requirements on the single measurements for tides and rotation are particularly challenging, especially for a mission such as UOP with multiple science objectives. Reaching similar relative precisions is already particularly ambitious even with a dedicated mission such as Europa Clipper, for which 49 flybys are planned (E. Mazarico et al. 2023). Furthermore, the determination of time-varying signals, such as tides, is inherently challenging owing to the low eccentricity of the Uranian satellites (e.g., Ariel's eccentricity is about 30 times smaller than that of Titan). In this section, we apply the reverse approach described in Section 2 to the five major Uranian satellites. As previously stated, we combine measurements of the MoI, k_2 Love number,

Table 2
Uniform Priors Used for Interior Parameter Space Sampling

		Unit	Miranda	Ariel	Umbriel	Titania	Oberon
Ice-I shell density	ρ_s	kg m^{-3}	700–1050	700–1050	700–1050	700–1050	700–1050
Water ocean density	ρ_o	kg m^{-3}	700–1050	700–1050	700–1050	700–1050	700–1050
Rocky core density	ρ_c	kg m^{-3}	2400–3500	2400–3500	2400–3500	2400–3500	2400–3500
Ice-I shell thickness	d_s	km	30–150	70–250	70–250	70–290	70–280
Water ocean thickness	d_o	km	0–100	0–100	0–100	0–100	0–100

Table 3
Expected Geodetic Observables for a Three-layer Interior with and without a Global Subsurface Ocean

		Unit	Miranda		Ariel		Titania	
			Oceanless	50 km Ocean	Oceanless	50 km Ocean	Oceanless	50 km Ocean
Moment of inertia	MoI		0.3409	0.3417	0.3123	0.3125	0.3116	0.3117
Love number	k_2		4.9×10^{-4}	2.52×10^{-3}	1.72×10^{-3}	2.03×10^{-2}	3.1×10^{-3}	3.99×10^{-2}
Libration amplitude	g_s	m	−48.29	−58.88	−21.46	−29.27	−2.27	−3.19
Obliquity	ε	m	84.6	83.6	7.6	7.5	186.9	262.7

Note. Ariel is a proxy for Umbriel, and Titania is a proxy for Oberon.

libration amplitude, and obliquity, along with the mass, in order to explore their combined sensitivity to the interior parameters and relax the stringent requirements reported in Table 1. In particular, we focus our discussion on the expected probability distribution of the ice shell thickness (d_s), ocean depth (d_o), and rock-to-ice mass ratio

$$\mathrm{rock/ice} = \frac{\rho_c R_c^3}{\rho_s (R_s^3 - R_o^3) + \rho_o (R_o^3 - R_c^3)}, \tag{2}$$

where the subscripts c, o, and s refer to silicate core, ocean, and ice shell quantities, respectively.

Synthetic "true" geodetic observables are computed for a set of interior models with d_o ranging from 0 to 50 km every 10 km. The core, ocean, and shell densities are fixed at 3060, 1000, and 950 kg m^{-3}, respectively (J. Castillo-Rogez et al. 2023). The core radius and ice shell thickness are computed in order to satisfy the mean satellite radius and mass. The shell and core are assumed to be elastic, with rigidity fixed to 3.3×10^9 Pa and 50×10^9 Pa, respectively (H. Hussmann et al. 2006). We do not vary ice shell rigidity and viscosity, as these have less influence on k_2 than ice shell thickness. The uniform prior distributions used for inversion, as shown in Table 2, are, to some extent, consistent with previous studies (H. Hussmann et al. 2006; C. J. Bierson & F. Nimmo 2022; J. Castillo-Rogez et al. 2023; R.-M. Baland et al. 2025).

The uncertainties associated with the synthetic geodetic observables are varied from 100% to 0.01% relative to the model true value, with the exception of the mass, for which a loose sigma of 1% is fixed for every run. This loose mass uncertainty strategy is commonly used to incorporate the inherent uncertainty associated with the interior model unknowns into the inversion process, thus preventing the potential issue of nonconvergence (see, e.g., G. Cascioli et al. 2024 for simulation or A. Genova et al. 2019 for real data analysis). This approach also yields more conservative results, thereby making it well suited for simulations at the initial stages of mission design. An uncertainty level of 100% generally means that the estimation of the geodetic observable has failed and that it provides no information about the internal structure. There may, however, be exceptions. For example, given the seemingly inverse relation between k_2 and shell thickness, an individual measurement of k_2 with a precision level above 100% can, for interiors with thick shells and therefore small k_2, provide a useful constraint on the thickness of the shell in the form of a lower bound. In some cases, the true value defining the 100% level is not always the maximum value within the range of model predictions. Instead, it can be observed to be relatively small in comparison to the range. Therefore, it should be kept in mind that requiring a measurement at signal level to constrain the interior does not always mean that the measurement is useless when considered in conjunction with other geodetic observables. Moreover, in certain instances, such requirements may still prove challenging, particularly when the absolute parameter values are very small. Specific cases are tested and discussed in detail in Section 3.1, and it is recommended to take a case-by-case approach in order to define the final instrument requirements.

Given that Ariel and Umbriel, on the one hand, and Titania and Oberon, on the other hand, have approximately the same size and mass and similar tidal and rotational responses (R.-M. Baland et al. 2025), we only discuss the results for Miranda, Ariel, and Titania. The last two will serve as proxies for Umbriel and Oberon, respectively. We discuss below the needed precision on the geodetic measurements (i.e., on MoI, k_2, g_s, and ε) relative to their true value, as predicted by the forward modeling and reported in Table 3 for a case with a 50 km ocean and for a case without. We do not give the true values for all the ocean thicknesses considered here, because the order of magnitude of the geodetic observables remains similar.

All the following results are based on the interpolation of our "lookup tables" that map the geodetic measurements' combinations to the interior parameters given a specific interior structure. Such measurements to interior mapping enable very rapid assessment of the geodetic measurement precision required to achieve a desired level of uncertainty of any interior parameter and therefore any interior objective. As the cases discussed in this paper in terms of interior parameter determination constitute only a handful among many possibilities (e.g., we did not investigate the determination of the individual densities of the different layers), we deliver our lookup tables (six per satellite, one for each ocean thickness considered here) as MRTs (see Appendix C). Readers can use them to construct their own tool in accordance with their specific requirements in terms of measurements and interior objectives. Note that these maps can also be used in reverse to determine how well interior properties can be constrained given four geodetic measurement uncertainties. This usage is demonstrated and discussed in Section 4.2.

3.1. Nominal Case (True Ocean Thickness = 20 km)

We first consider a nominal case for which the "true" thickness of the ocean is fixed at 20 km. J. Castillo-Rogez et al. (2023) do not predict an ocean thicker than 30 km for Ariel and Umbriel and 50 km for Titania and Oberon, so a thickness of 20 km can be used as a reference case for the medium-sized satellites. Although Miranda is not thought to harbor a global subsurface ocean, we are nevertheless exploring this possibility here.

Figure 1 shows the combinations of geodetic measurement precisions relative to the model true value necessary to determine the ocean thickness (d_o), the rock-to-ice mass ratio (rock/ice), and the ice shell thickness (d_s) within a specified uncertainty level (from 5% to 30%) assuming that the satellites have an ocean of 20 km thickness. The rock-to-ice mass ratio uncertainty is calculated from the a posteriori distribution of the core (ρ_c), ocean (ρ_o), and ice shell (ρ_s) densities and of the core (R_c), ocean (R_o), and ice shell (R_s) radii using Equation (2). There are multiple ways to select combinations of geodetic measurement uncertainties that give the same result in terms of interior parameter uncertainties. Here we discuss combinations that are obtained such that the (σ_{MoI}, σ_{k_2}, σ_{g_s}, σ_{ε}) quadruplet maximizes the Euclidean (L2) norm. In other words, we choose the combinations that require the loosest constraints across all four geodetic measurements.

Ocean thickness. For all the satellites, determining the thickness of the ocean to an accuracy of 30% requires a combination of MoI, k_2, and libration measurements with an uncertainty equal to or less than 1% and an obliquity measurement with a looser uncertainty, which may be at the signal level for Miranda. For Ariel, the obliquity measurement is required with an absolute precision of 0.25 m, whereas the MoI, k_2, and g_s must be determined with absolute precisions of 9.2×10^{-4}, 1.4×10^{-4}, and 0.24 m, respectively. Overall, the ocean thickness is more challenging to determine than the rock-to-ice mass ratio and ice shell thickness (see below). It is worth mentioning that measuring the ocean thickness at the 5% level for Miranda is not feasible without relative uncertainties that are smaller than 10^{-4} (no blue polygon on the left panel of Figure 1(a)).

Rock-to-ice mass ratio. For Miranda, a relative uncertainty level of 30% on the rock-to-ice mass ratio can be achieved by measuring the MoI with a precision of the order of one percent (so 7.95×10^{-3} in absolute) along with a determination of the k_2 Love number, obliquity, and libration amplitude at the signal level (so 1.5×10^{-3}, $0\overset{\circ}{.}015$, and ~$0\overset{\circ}{.}0002$, respectively). From a dedicated MCMC analysis where only the MoI measurement is considered, we find an uncertainty of 34% on the rock-to-ice mass ratio. Therefore, the 100% required levels on k_2, obliquity, and libration mean that these parameters barely contribute to the constraint on the rock-to-ice ratio with an equivalent 30% uncertainty. Ariel (Umbriel) requires similar measurement requirements to those of Miranda for obliquity and k_2, both at the signal level (i.e., 7.4 m and 1.6×10^{-02} in absolute, respectively). However, the measurement at the percent level of libration (2.8 m in absolute) is required instead of the MoI measurement. The same relative precisions are needed for Titania (Oberon), corresponding in absolute to 0.8 m on g_s, 0.3 on the MoI, 0.003 on k_2, and 162 m on ε. The latitude we gain in determining the MoI for Ariel and Titania comes at the expense of the precision needed in determining g_s (a dedicated MCMC analysis indicates the same trend as discussed for Miranda). To reach an uncertainty of the order of 5% or better on the rock-to-ice mass ratio, it is necessary, for Miranda and Ariel, to determine the four geodetic observables with a precision $\leqslant$1% of the signal level. In the case of Titania, however, the same precision is achieved with the measurement of obliquity and MoI at the signal level.

Ice shell thickness. The ice shell thickness d_s is the less challenging interior parameter to constrain from the geodetic observables. It can be determined with an uncertainty of 30% or 20% by measuring the four observables at the signal level for all satellites. This illustrates how sometimes an observable with 100% uncertainty is still necessary to infer an interior parameter (just because it provides an upper bound for its true value). Generally speaking, MoI and ε are less sensitive to d_s than k_2 and g_s, as expected from theory (R.-M. Baland et al. 2025). For Ariel and Titania, MoI and ε are not even needed to still measure d_s with 10% precision. If one wants to be more precise and get d_s with 5% uncertainty, then MoI and obliquity need to be determined to a few percent. For Miranda, k_2 drives the uncertainty level on d_s, while the libration is the main driver for the determination of d_s for Titania (Oberon). For Ariel (Umbriel), k_2 is not contributing and g_s is the most influencing observable among the other three.

3.2. Sensitivity to Ocean Thickness

The results described above are based on a truth model with $d_o = 20$ km. The impact of this assumption on the results has been tested and is shown in Figure 2 for Ariel only (as the behavior is the same for all moons), where we vary the thickness of its ocean from 0 to 50 km. As we are interested in the impact of the value of the "true" d_o on the required precisions, we show here the ratio of the latter with respect to their value in the nominal case ($d_o = 20$ km), presented in Figure 1. We see in Figure 2 that the actual ocean thickness (i.e., the "true" d_o in the x-axis) mostly impacts the required uncertainties to determine d_o itself (top panel). The thinner the ocean, the more precise the geodetic observables must be to reach a given level of precision on d_o. This is not true for the other two interior parameters, d_s and rock/ice, for which the required uncertainties vary less with d_o and do not always increase with it (see the middle and bottom panels of Figure 2).

3.3. Combinations from a Subset of Geodetic Observables

It is important to note that there exists a multitude of combinations of MoI, k_2, g_s, and ε that allow the determination of an interior parameter below a desired degree of precision. Some of these combinations could be seen (from the mission design point of view) as particularly interesting since they do not require all four geodetic observables to be determined at a precision better than 100%. Most of the time (but not always, as discussed above for d_s at 20%–30%) this means that one (or

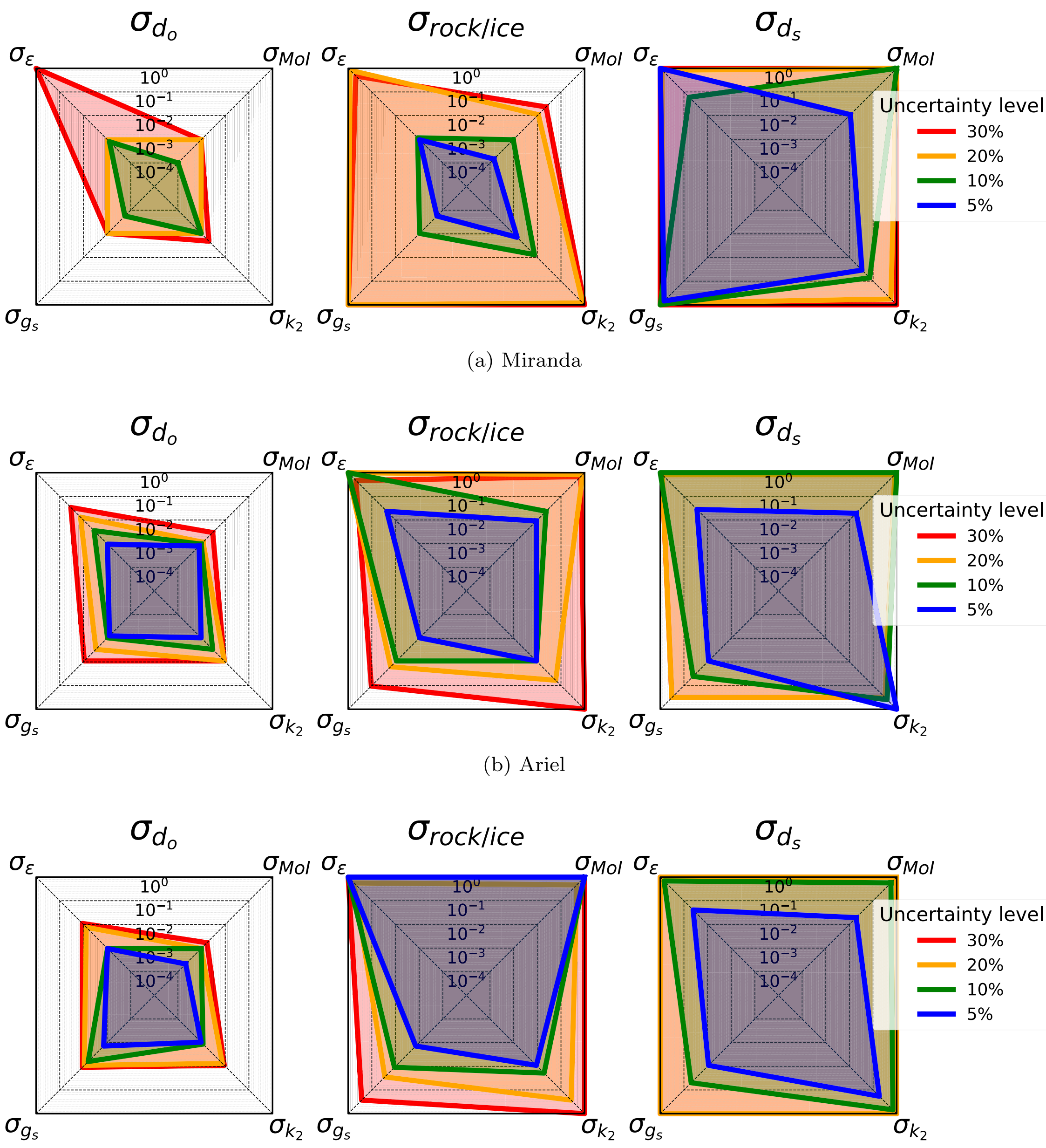

(a) Miranda

(b) Ariel

(c) Titania

Figure 1. Combinations of measurement relative precisions allowing us to measure the ocean thickness (d_o), the rock-to-ice ratio (rock/ice), and the ice shell thickness (d_s) with a given uncertainty level when the satellites have an ocean of 20 km depth. The combinations shown are the ones that have the maximum L2-norm (loosest measurement requirements) and that achieve the desired level of uncertainty.

more) observables are basically not systematically needed, which can simplify the operations. For instance, if the libration is not needed to reach the targeted uncertainty on the interior of one of the satellites (e.g., for d_s of Miranda), then one can use the camera for another purpose. We show some of these particular combinations in Figure 3. Their number depends on the interior parameter and the body considered. For example, there are more of these combinations that lead to a 5% uncertainty estimate of Miranda's ice shell thickness than for Ariel and Titania. With regard to the last two, we only found one quadruplet that allows us to determine d_o with a precision of 30% with one geodetic parameter determined with 100% uncertainty (e.g., for Titania a relative precision of about 10^{-3} is required for σ_{MoI} and σ_ε, 10^{-2} for σ_{k_2}, whereas libration can be determined to signal level). As might be expected, relaxing the needed uncertainty on a given observable results in an increase in the precision needed on the others, as clearly shown in Figure 3. It seems also that such a trade-off is "observable dependent," meaning that a given observable will preferably compensate for another one specifically. For instance, libration and k_2 tend to compensate each other.

3.4. Simultaneously Achieving Different Interior Objectives

So far, we have been selecting the geodetic measurement precision quadruplets such that one specific interior parameter can be determined with a given level of uncertainty. We now discuss the case where the interior parameters (d_o, rock/ice, d_s) are simultaneously estimated at the same relative level of precision. As previously, our truth model assumes $d_o = 20$ km, and we

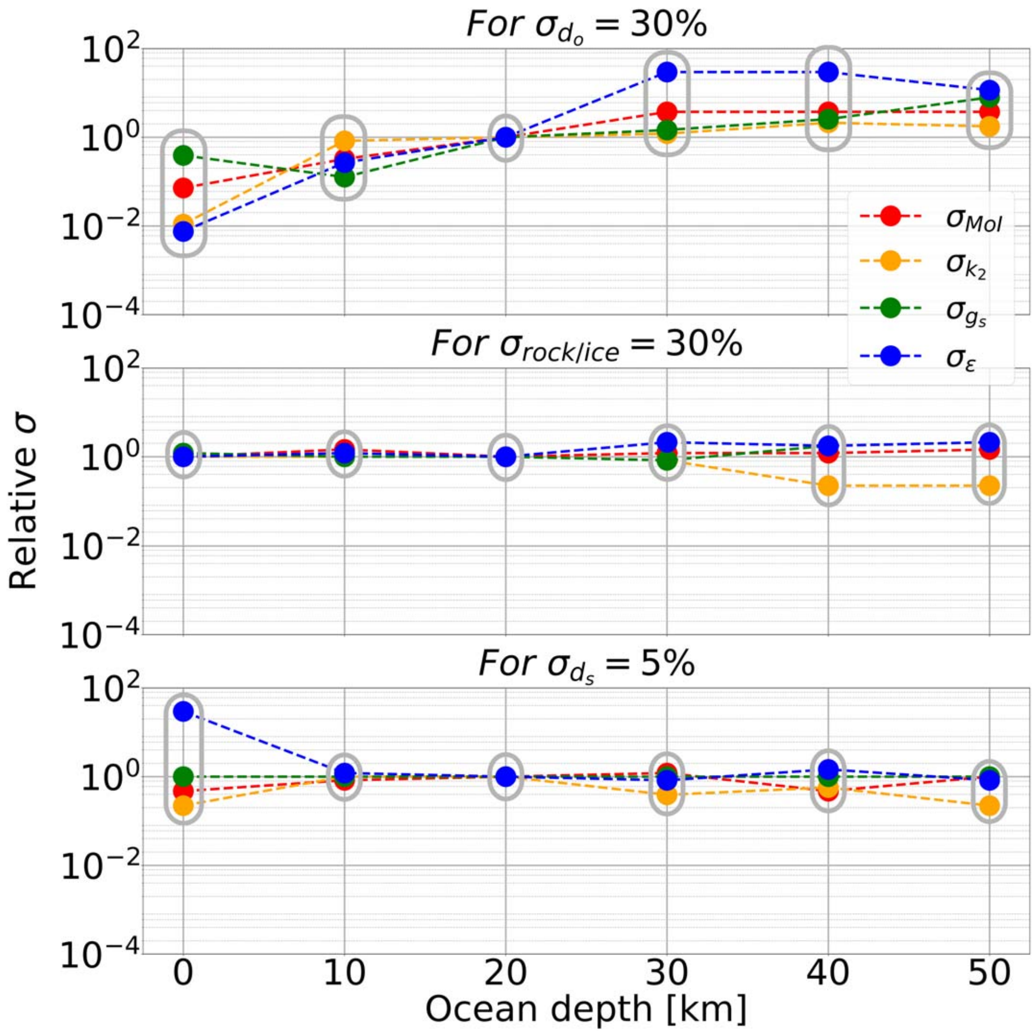

Figure 2. Ocean thickness dependence of required precision quadruplets (marked with gray frames) in Ariel's geodetic observables, relative to our $d_o = 20$ km nominal case. These uncertainties in the MoI, k_2, g_s, and ε are selected such that one can determine the ocean thickness itself (d_o) and the rock-to-ice ratio (rock/ice) at the 30% level and the ice shell thickness (d_s) at the 5% level. For the case with no ocean ($d_o = 0$ km), the $\sigma_{\rm MoI}$, σ_{k_2}, σ_{g_s}, and σ_ε are selected such that d_o can be inferred with an uncertainty of 30 km, which makes this case not readily comparable to the others, but nonetheless quite instructive. The quadruplets are the ones with the maximum L2-norm among all possible combinations.

target an uncertainty on all three interior parameters at 30%. Figure 4 shows how challenging it is to precisely measure d_o, rock/ice, and d_s at once, in particular for Titania, where all four geodetic parameters must be determined with 1% uncertainty or better. Even for the case with only 30% uncertainty on d_o, rock/ice, and d_s, one would need to measure the geodetic parameters of Miranda with the following formal errors: $\sigma_{\rm MoI} = 1.5 \times 10^{-3}$, $\sigma_{k_2} = 6.5 \times 10^{-6}$, $\sigma_{g_s} = 0.2$ m, and $\sigma_\varepsilon = 9$ m. For Ariel (Umbriel) the required uncertainties would be $\sigma_{\rm MoI} = 5 \times 10^{-4}$, $\sigma_{k_2} = 1.5 \times 10^{-4}$, $\sigma_{g_s} = 0.2$ m, and $\sigma_\varepsilon = 4.5$ m, and for Titania (Oberon) we would need $\sigma_{\rm MoI} = 5 \times 10^{-4}$, $\sigma_{k_2} = 3 \times 10^{-4}$, $\sigma_{g_s} = 3.5 \times 10^{-2}$ m, and $\sigma_\varepsilon = 3$ m. This will be almost unachievable with UOP as discussed in the next section and as we can anticipate given the level of precision obtained on Titan's geodetic parameters from 10 Cassini flybys (D. Durante et al. 2019; S. Goossens et al. 2024). This means that one might have to decide which of the three interior parameters really needs to be measured with good precision and which may not.

There are very few subsets of geodetic observables where at least one observable is measured at the signal level while allowing us to determine all three interior parameters simultaneously with needed uncertainty without requiring the other observables to be measured with extremely high precision ($\leqslant 10^{-4}$). Figure 5 illustrates four potential combinations that enable the simultaneous determination of all three interior parameters at the 30% (top), 20% (middle), or 10% (bottom) level of precision. These combinations are characterized by one geodetic measurement having the loosest requirement, with the additional constraint that the other geodetic measurements should have a relative uncertainty $\geqslant 10^{-3}$. Reaching the 10% precision level on the three interior parameters of Ariel does not allow us to loosen any geodetic observable significantly compared to the 10^{-3} threshold. That level of uncertainty on d_o, rock/ice, and d_s cannot even be reached for Titania and Miranda under these conditions, and the looser 20% level is still not achievable for the latter. Even at 30%, only libration (for Titania) or obliquity (for Ariel) can be relaxed to signal level, requiring then the other three to be measured at the 10^{-3} threshold level. For all other cases, the four geodetic observables must all have a relative precision better than 10% to reach the target uncertainty on d_o, rock/ice, and d_s.

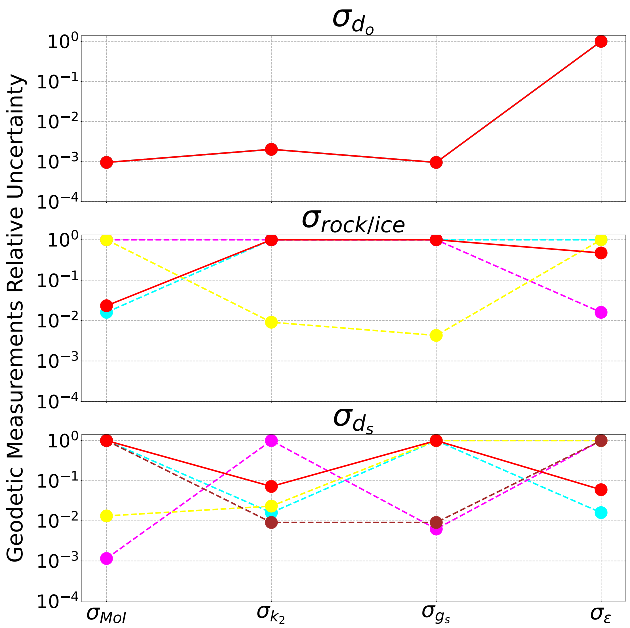

(a) Miranda

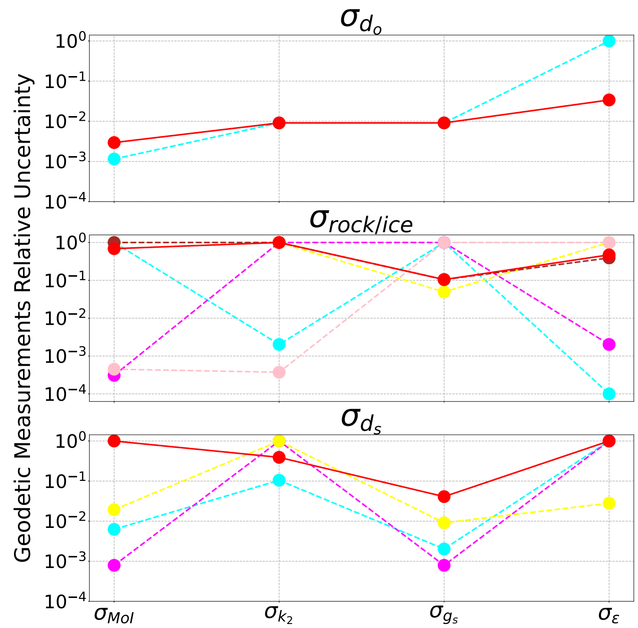

(b) Ariel

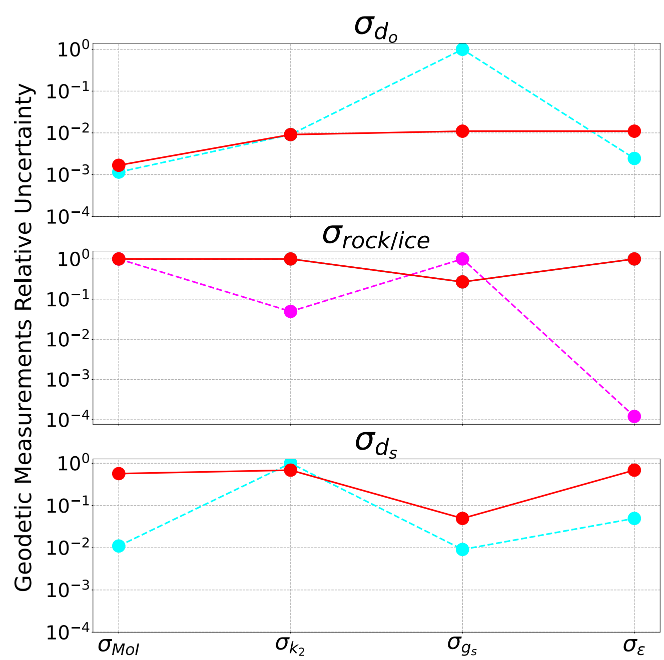

(c) Titania

Figure 3. Alternative quadruplets allowing us to measure the ocean thickness (d_o) and the rock-to-ice mass ratio (rock/ice) with a 30% uncertainty level, and the ice shell thickness (d_s) at 5% when the satellites have an ocean of 20 km depth. These combinations all have one or more geodetic parameters with 100% uncertainty. Each colored dotted line represents a quadruplet. The red solid lines indicate the solutions presented in Figure 1 for the nominal case.

4. A Backward Application Framework: From GS Experiment Design to Interior Structure Objectives

In this section, we analyze the ability of the UOP GS experiment designs to fulfill the mission's scientific objective regarding the interior properties of the Uranian satellites, as outlined in Section 3. The POD of the spacecraft usually relies on range and range-rate radiometric observations collected by the GS experiment of the mission to precisely reconstruct the spacecraft's trajectory, with the ultimate goal of constraining the interior structure of the body through the precise determination of its gravity field. The interior structure of a planet can also affect its rotation and orientation in space, but these are difficult to measure using radiometric data alone, especially from flybys (e.g., D. Durante et al. 2019; E. Mazarico et al. 2023). In such a case, and therefore in particular for the UOP mission, landmark tracking from

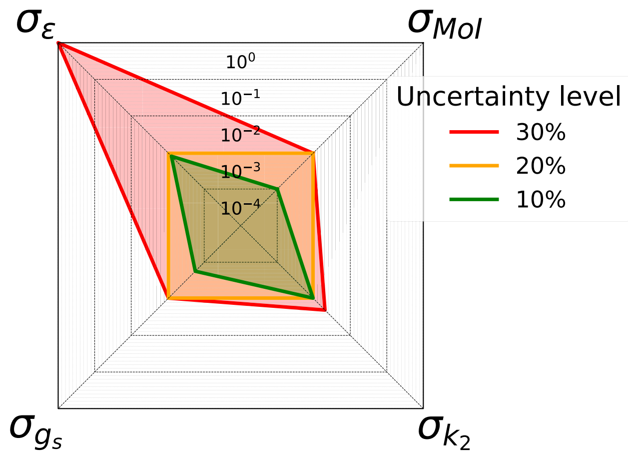

(a) Miranda

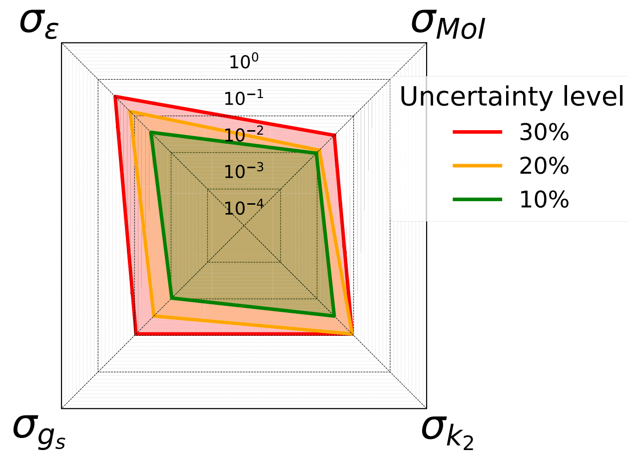

(b) Ariel

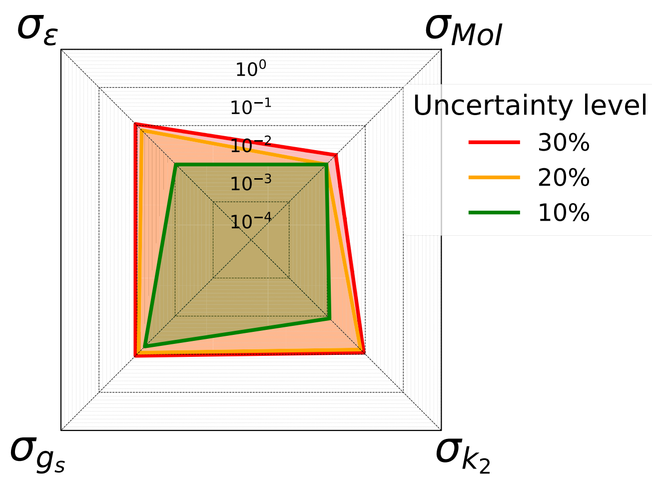

(c) Titania

Figure 4. Required relative precisions on MoI, k_2, g_s, and ε to determine all three interior parameters (d_o, rock/ice, and d_s) with a specified degree of uncertainty for a satellite with an ocean depth of 20 km. The relative precisions are set to be equal for each interior parameter. The combination shown is the one with the maximum L2-norm among all possible combinations.

spacecraft image data is required to precisely measure the body's rotational parameters (e.g., A. S. Konopliv et al. 2014; P. Thomas et al. 2016; R. S. Park et al. 2024).

The POD approach refines the spacecraft's dynamical model by comparing synthetic data, derived from both dynamical and observational models, with simulated measurements. A weighted least-squares filter is used to improve the knowledge of the spacecraft's initial state vector and other variable parameters in the model, such as the gravity spherical harmonic coefficients. The goal is to minimize the sum of squared residuals between the synthetic data and the simulated measurements. An in-depth description of the POD least-squares technique can be found in B. D. Tapley et al. (2004), whereas the landmark tracking technique used to process optical data is described in, e.g., R. S. Park et al. (2020).

First, we conduct a covariance analysis to assess the ability of radiometric and landmark tracking data from the UOP's satellite tour to infer the geodetic parameter of interest, namely $\sigma_{\rm MoI}$, σ_{k_2}, σ_{g_s}, and σ_{ε}. Full details about our POD simulations are discussed in Appendix A. Section 4.1, as well as Table 4, summarizes the most important aspects of the simulated GS experiment designs. Second, the GS experiment designs are evaluated in terms of their capacity to infer the interior properties of the Uranian satellites, using the lookup tables computed in Section 3.

4.1. POD Simulation Settings

We analyze the expected performance of two distinct orbital tours: the Decadal Tour, as recommended by the Planetary Science and Astrobiology Decadal Survey, and an Alternative Tour, which includes a minimum of two close flybys per moon and a more diverse flyby geometry (see Figure 6 and Appendix A.1 for more details). The latter tour also provides an enhanced temporal sampling (that is, flybys of the satellite at varying mean anomalies with respect to its primary), which is essential for accurately measuring signals at orbital frequencies.

Synthetic coherent two/three-way direct-to-Earth-link Doppler and optical point image measurements are generated using the NASA-JPL orbit determination software MONTE (S. Evans et al. 2018) as detailed in Appendix A.2. Given that the mission design is still in its preliminary stages, we conducted a series of tests to consider a range of GS experiment capabilities within the context of the Uranian system. In particular, the performance of the X band and that of

Table 4
Characteristics of the Gravity Science Experiments Tested in This Study

Setting	Values
Orbital tour	Decadal; Alternative
Data type	Radiometric; radiometric+optical
Radio link	X band; Ka band
Tracking pass duration	1, 2, 4, and 6 hr
Pictures per flyby	2, 4, 6, and 8
Landmarks per picture	5, 10, 30, and 50
Gravity field	From J_2 and C_{22} only, to full degree 3/4*
Body-fixed frame	α, δ, $\dot{W}$
Libration	g_s
Tides	k_2

Note. The geodetic parameter sets, including gravity, frame, tides, and libration, are combined with the base set described in Section 4.1. These parameter sets are tested using multiple measurement strategies and tour configurations, defining the explored parameter space. Each case is evaluated with and without the hydrostatic constraint ($J_2/C_{22} = 10/3$). An asterisk indicates degree and order 3×3 for Miranda, Umbriel, and Oberon and degree and order 4×4 for Ariel and Titania.

the Ka band are evaluated separately, with tracking durations varying from 1 to 6 hr around the closest approach (C/A).[5] With regard to the optical data, we examine the impact of the number of landmarks observed per image (5, 10, 30, and 50) and the number of images per flyby (2, 4, 6, and 8). The state-of-the-art noise levels utilized in this study are 0.1 mm s^{-1} for the X/X link and 10 μm s^{-1} for the Ka/Ka link over an integration time of 60 s for radiometric measurements (S. W. Asmar et al. 2005) and 2″ for optical measurements, which could be achieved, e.g., with a conservative $\sigma = 1$ pixel on 2″ pixels, or more typically $\sigma = 0.25$ pixels on 8″ pixels (R. T. Pappalardo et al. 2024; R. S. Park et al. 2024).

The expected uncertainties (1σ formal errors) of the estimated parameters in our POD solutions are calculated by processing the aforementioned synthetic measurements with a multiarc approach (A. Milani & G. Gronchi 2009). This approach allows us to employ relatively simple dynamical models (gravity and solar radiation pressure (SRP)) while still providing realistic and not overly optimistic estimation of the formal errors. For a comprehensive account of the underlying dynamical models, the reader is directed to Appendix A.3. A baseline set of parameters is always included. This set consists of the spacecraft state (one per flyby), the satellite *GM*, a minimal combination of gravity coefficients (J_2 and C_{22}), and one SRP scaling factor per arc. When optical data are also used, the baseline configuration is expanded to include camera pointing errors in the camera frame and the position of the landmarks (in latitude, longitude, and radial coordinates for each landmark). A number of parameter sets are evaluated by combining the described base set with one or more geodetic parameters, including gravity, frame, tides, and libration, as defined in Table 4. Furthermore, the impact of applying a hydrostatic constraint ($J_2/C_{22} = 10/3$, where J_2 and C_{22} are unnormalized) on the POD solutions is evaluated.

5 It is assumed here that the UOP will have Ka-band uplink capabilities, as the final experiment configuration is not yet clear (A. Simon et al. 2021), and that media calibrations and dual-link corrections can be applied.

4.2. Case Study: Ariel

As mentioned earlier, the approach presented in Section 2 can be utilized not only to determine the necessary geodetic measurement uncertainties to achieve a specific scientific objective, as illustrated in Section 3, but also to rapidly assess the performance of a POD solution in terms of interior parameter estimation. By testing POD performances for just two different orbit tours and a handful of measurement strategies and filter settings (see Table 4), we have already performed no less than approximately 15,000 simulations per satellite. It is impractical to perform an MCMC simulation for each POD solution, as there are too many of them and the process would be unfeasibly time-consuming. The mapping method described in Section 2, on the other hand, can very quickly assess the performance of each POD solution in its ability to constrain the interior parameters, simply by extracting/interpolating the corresponding interior parameter uncertainties from the lookup table. In this section, we apply this reverse approach to Ariel in order to define requirements for the mission design (instrument and operations) needed to achieve the mission's scientific objectives. We first validate our mapping method in Section 4.2.1. Subsequently in Section 4.2.2, we discuss the results of the covariance analysis with respect to the single measurement requirements shown in Table 1 and with respect to the uncertainties on the ocean and ice shell thicknesses and on the rock-to-ice ratio from the combined measurements. A comprehensive sensitivity analysis, which details the effects of various measurement strategies and the influence of the estimated parameter set on the uncertainties associated with geodetic and interior parameters, can be found in Appendix B. Furthermore, the same appendix provides the interested reader with the results of the sensitivity analysis for Miranda, Umbriel, Titania, and Oberon.

4.2.1. Mapping Method Validation

The reliability of our mapping method can be demonstrated by comparing the interior parameter uncertainties interpolated from the lookup table with those resulting from a dedicated MCMC run. We do so for the specific GS experiment design characterized by the Alternative Tour, 4 hr of tracking time centered on the C/A, Ka-band radiometric data, and optical data made of four pictures per flyby with 10 landmarks per picture. This experiment configuration was found to have sensitivity to all key measurements (MoI, libration, tides, and obliquity), and thus our POD estimated parameter set includes all of them, as well as the degree-two gravity coefficients J_2 and C_{22}. This specific simulation results in the following uncertainties in Ariel's geodetic parameters of interest: $\sigma_{\mathrm{MoI}} = 2.2 \times 10^{-5}$, $\sigma_{\varepsilon} = 5.3$ m, $\sigma_{g_s} = 1.8$ m, and $\sigma_{k_2} = 1.6 \times 10^{-2}$. Propagating the latter to the interior parameters by using our mapping method, we get $\sigma_{d_o} = 25.74$ km, $\sigma_{d_s} = 24.56$ km, and $\sigma_{\mathrm{rock/ice}} = 0.27$. As previously stated in Section 2, the uncertainty of an interior parameter is defined as half of the range between the 15.87th and 84.13th percentiles. In order to predict possible posteriori distributions that are flat, the noninformative constraint is not applied in this instance, prior to interpolation.

These interior parameter uncertainties are in fairly good agreement with the 15.87th and 84.13th percentile ranges reported at the top of Figure 7, which result from a dedicated MCMC run. We can see, in fact, that the highest relative error

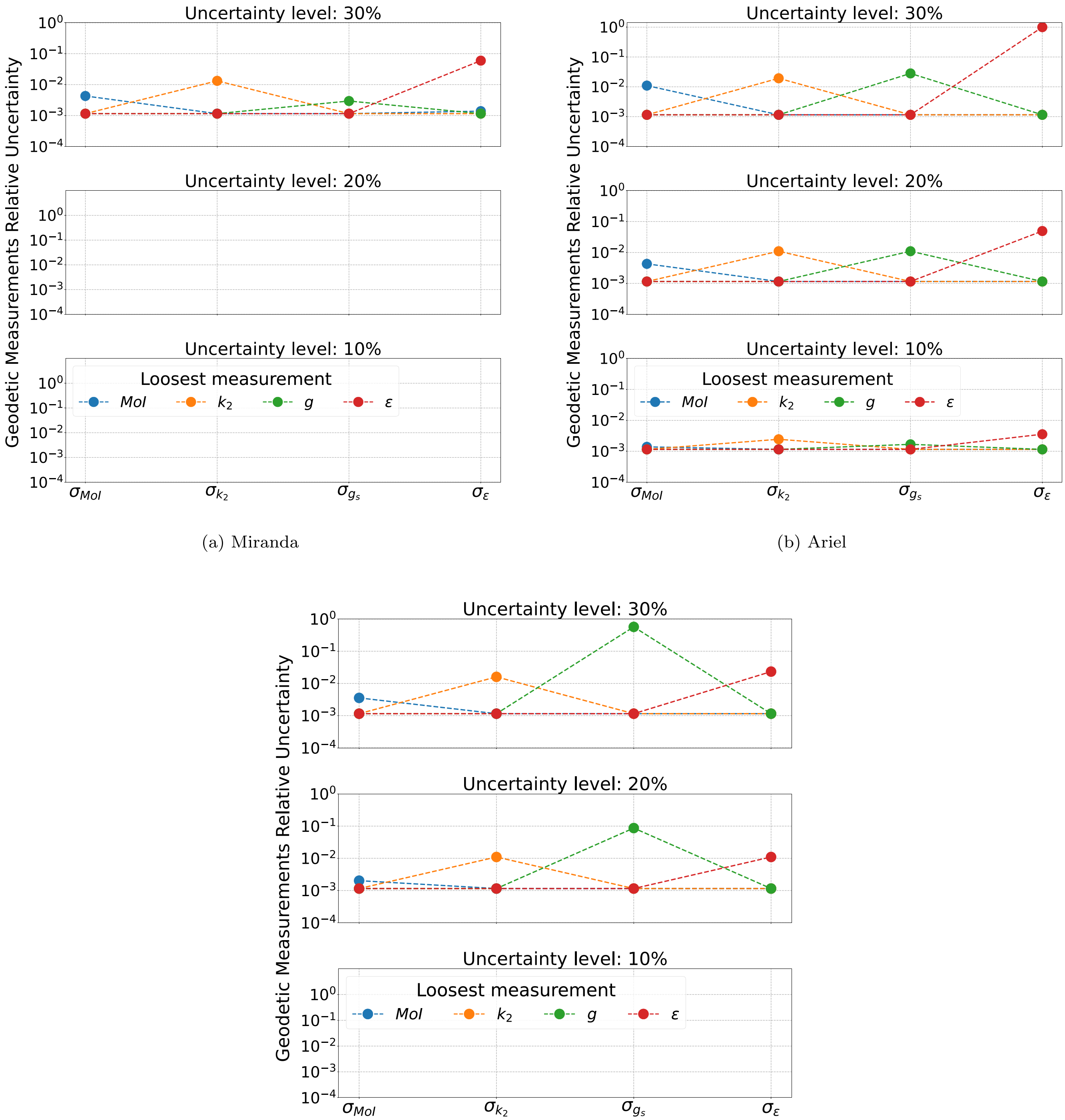

(a) Miranda (b) Ariel

(c) Titania

Figure 5. Alternative measurement combinations to determine together the three internal parameters (ocean thickness (d_o), rock-to-ice ratio (rock/ice), and ice shell thickness (d_s)) with a specified degree of uncertainty for a satellite with an ocean depth of 20 km. These combinations are characterized by one observable having the loosest possible requirement, whereas the others have a requirement greater than 10^{-3}. The absence of lines indicates that no combination has been identified.

of the mapping method, amounting to ~11%, is observed for the rock/ice uncertainty. The ocean and ice shell thicknesses, in contrast, show a relative error of 0.1% and 3%, respectively. This gives us confidence in the preliminary evaluations obtained with our mapping method on the POD solutions, which we discuss below. Note that the mapping method results remain an approximation and that we recommend running a full MCMC once the GS experiment design has been chosen.

4.2.2. UOP Mission Requirements for Interior Determination

In a POD solution, the set of estimated parameters significantly impacts the estimated formal errors associated with the investigated parameters. The determination of the appropriate parameter set is contingent on the data at hand (i.e., the final trajectory, instrumentation, and observation strategy). Consequently, it is not possible to make an informed choice at this stage of the mission design process. Moreover, even when

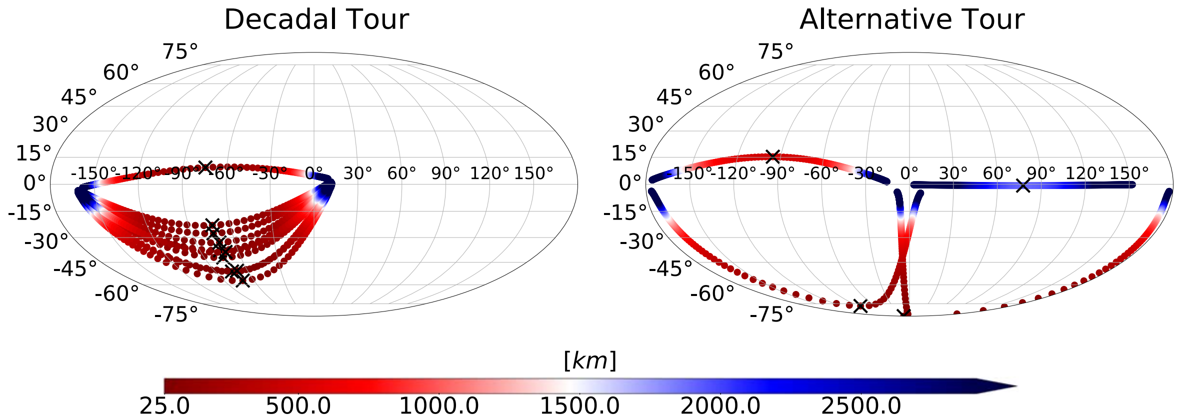

Figure 6. UOP flybys of Ariel (±30 minutes around C/A). Colors show the altitude with respect to the moons' surface, whereas the crosses show the point of C/A. Only flybys with a C/A distance less than three body radii are shown.

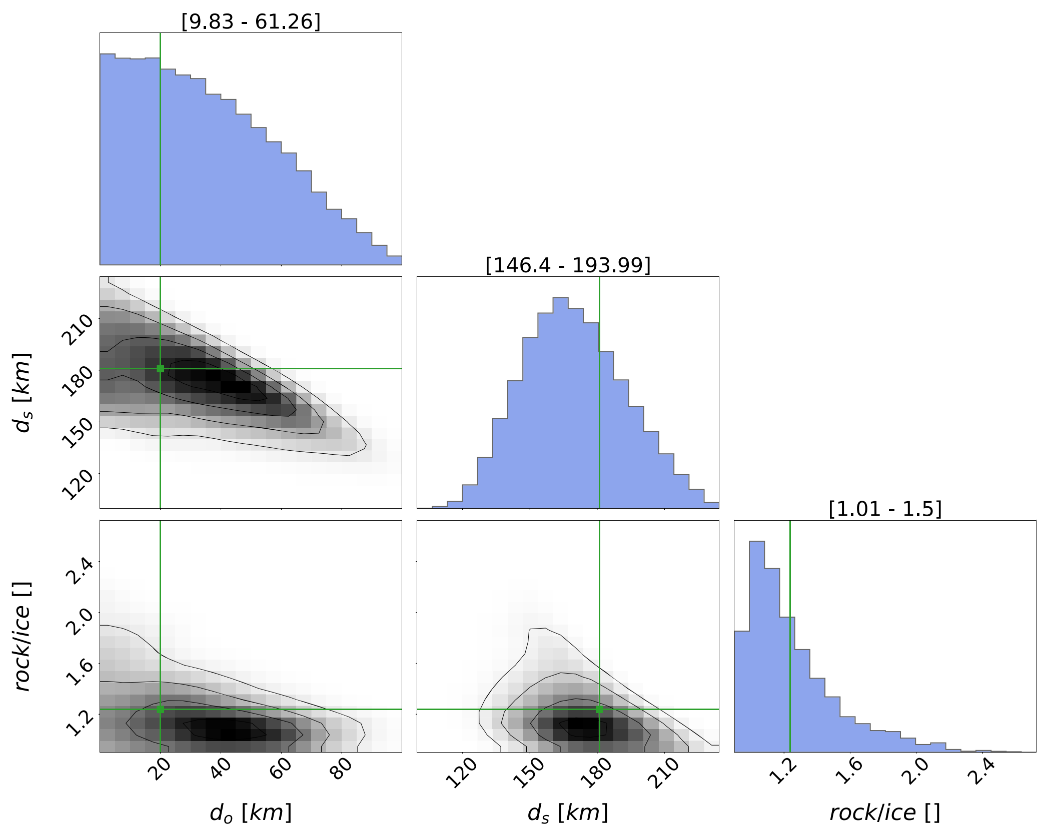

Figure 7. Posterior distributions of Ariel's interior parameters, derived from a dedicated MCMC run (50 walkers, 100,000 steps). The uncertainty on the geodetic observables (MoI, k_2, ε, and g_s) was quantified using covariance analysis. This POD solution was characterized by the Alternative Tour, 4 hr of tracking time around C/A, radiometric (Ka band), and optical (four pictures per flyby, 10 landmarks per picture). The titles show the 15.87th and 84.13th percentiles of the posterior distributions, which correspond to the following uncertainties as defined in Section 2: $\sigma_{d_o} = 25.72$ km, $\sigma_{d_s} = 23.80$ km, and $\sigma_{\mathrm{rock/ice}} = 0.25$. Green points show the truth values.

the mission design is finalized, detailed numerical simulations (perturbative, robustness analysis, etc.) will need to be run for each candidate tour to assess the optimal parameter set, that is, the one that captures all the effects without overparameterizing the solution. Our mapping method provides a solution to this problem during the early stages of the mission design process, allowing for direct testing of the impact of different measurement strategies and estimated parameter sets on the determination of the interior parameters of interest, such as ocean and ice shell thickness and the rock-to-ice ratio, as demonstrated in Appendix B. Furthermore, a plausible estimated parameter set can be postulated based on an analysis of past GS experiments (e.g., degree and order 5 × 5 and k_2 of Titan with 10 flybys, S. Goossens et al. 2024; body-fixed frame and libration amplitude from optical measurements, S. Burmeister et al. 2018; R. S. Park et al. 2024). The Decadal Tour provides 12 close flybys (i.e., flybys with a C/A ratio less than three times the body's radius) of Ariel, whereas the Alternative Tour provides only four, but with an improved spatial coverage (see Appendix A.1 for details). A sensitivity analysis of the gravity

Table 5
Minimum Requirements for Radiometric (Ka Band) and Optical Measurements to Meet the Specified Target Uncertainties for the Geodetic Parameters of Ariel Presented in Table 1

	Parameter Set	Decadal Tour			Alternative Tour		
		Track. Time (hr)	Pictures	Landmarks	Track. Time (hr)	Pictures	Landmarks
MoI	$sh3 + \epsilon + g_s$	1	2	5	1	2	5
	$sh3 + \epsilon + g_s + k_2$	6	4	10			
	$sh4 + \epsilon + g_s$	1	2	5	1	2	5
	$sh4 + \epsilon + g_s + k_2$	6	6	10			
k_2	$sh3 + \epsilon + g_s + k_2$	6	4	10			
	$sh4 + \epsilon + g_s + k_2$	6	6	10			
g_s	$sh3 + \epsilon + g_s$	1	4	10	1	2	5
	$sh3 + \epsilon + g_s + k_2$	6	6	10			
	$sh4 + \epsilon + g_s$	4	4	10	1	2	5
	$sh4 + \epsilon + g_s + k_2$	6	6	10			
ε	$sh3 + \epsilon + g_s$	1	4	50	1	6	5
	$sh3 + \epsilon + g_s + k_2$	1	4	50			
	$sh4 + \epsilon + g_s$	1	4	50	1	6	5
	$sh4 + \epsilon + g_s + k_2$	4	4	50			

Note. The target uncertainty for the k_2 Love number represents the most optimistic target uncertainty for ocean detection, given that all other targets for k_2 have not been met by any of the tested strategies. The total tracking time around C/A is defined as the tracking time in hours. The number of pictures is the total number of pictures per flyby, whereas the number of landmarks is the number of landmarks per picture.

error spectra indicates that the maximum resolvable spherical harmonics degree and order is 3 × 3 for the Alternative Tour or 4 × 4 for Decadal Tour, given our truth gravity field (as defined in Appendix A.3). The use of optical data may facilitate the estimation of the satellite's rotational state, thereby enabling the determination of its obliquity and libration amplitude. The determination of tides, however, is a more challenging process owing to the necessity of both spatial and temporal coverage. Libration amplitude can also be more accurately determined with complete temporal coverage.

In order to discuss the expected uncertainties on the geodetic and interior parameters, we rule out right from the start POD solutions that poorly constrain all the geodetic parameters. In practice, that means that we ignore all solutions where the four geodetic parameter uncertainties (σ_{MoI}, σ_{k_2}, σ_{g_s}, and σ_{ε}) are above 100% of their nominal values (see Appendix A.3). From the total of ≈25,000 simulations for Ariel, approximately 42% of the solutions satisfy this condition. We discuss here the required measurement strategies for the two tested tours, assuming the availability of Ka/Ka Doppler and optical data and a parameter set comprising libration amplitude, obliquity, and gravity field coefficients up to degree and order 3 × 3/4 × 4. Note that considering correlations with higher-degree coefficients (up to 6) does not alter our conclusions as discussed in Appendix B. Additionally, we will discuss the measurement requirements for an inversion strategy that includes tides, in combination with the aforementioned parameters.

Table 5 summarizes the minimum observation strategy for the two investigated tours and for the aforementioned parameter sets that allows us to meet the target uncertainties shown in Table 1. In order to determine Ariel's hydrosphere thickness at the ±50 km level of precision, its MoI must be determined with an uncertainty of $\sigma_{\mathrm{MoI}} \leqslant 0.005$, which can be achieved using both tours with 1 hr of tracking time, two pictures per flyby, and five landmarks per picture, when estimating the gravity field up to degree and order 3 × 3 or 4 × 4 and rotation parameters, but not tides. It is a challenging task to properly measure the k_2 Love number and achieve the target uncertainty shown in Table 1. In fact, the necessity to solve for k_2 demands 6 hr of tracking time, four pictures per flyby, and 10 landmarks per picture for the Decadal Tour if degree and order 3 × 3 gravity field coefficients and rotation parameters are estimated. If the gravity of degree and order 4 × 4 is included, two additional pictures per flyby are required to meet the target uncertainties of both MoI and tides. Love number k_2 cannot be estimated to the required level with the Alternative Tour. The greater diversity and variety of flyby geometries, coupled with an improved temporal sampling of the Alternative Tour, permit the determination of the libration amplitude and obliquity with an uncertainty of 1 and 5 m, respectively, despite the reduced number of flybys (see Appendix A.1 for a detailed description of the two tours). Specifically, only two pictures per flyby and five landmarks per picture are needed instead of four and 10 for g_s, while six pictures and five landmarks are needed instead of four and 50 for ε.

As illustrated in Table 5, the Alternative Tour is unable to adequately constrain Ariel's k_2 Love number, which significantly limits its capacity to constrain the interior parameters. Consequently, the subsequent discussion focuses on the Decadal Tour unless otherwise stated. There are only a handful of solutions that can constrain the ocean thickness with a relative uncertainty better than 100%. The best relative uncertainty among the tested cases is 92% and can be achieved by the observation strategy that maximizes the number of measurements (i.e., 6 hr, eight pictures, and 50 landmarks) and fitting the gravity field to a maximum degree and order equal to 3. According to Section 3, d_o should be more challenging to constrain than d_s and the rock-to-ice mass ratio. Indeed, the rock-to-ice mass ratio can be constrained with a relative uncertainty of about 28% with 6 hr Ka tracking around C/A, four pictures per flyby, and 10 landmarks per picture when the maximum degree and order 3 spherical harmonics are estimated. Two additional pictures are required when the considered gravity degree and order are equal to 4. It was not possible to constrain the rock-to-ice mass ratio with an uncertainty level better than 21% using any of the tested measurement strategies. We confirm that d_s is the most easily constrained of the interior parameters discussed in this study. Our findings indicate that 6 hr Ka-band tracking, four (six) pictures per flyby, and 10 landmarks per picture can constrain the ice shell thickness at the 16% level if gravity of degree and order 3 (4) is included. A similar degree of uncertainty on d_s can be attained by reducing the tracking time and increasing the number of optical measurements, which will result in a less precise determination of k_2 but a more accurate determination of g_s. This is because these two factors offset each other with regard to the determination of d_s (see Section 3.3). It is noteworthy that a comparable level of uncertainty on rock/ice and d_s can be achieved by the Alternative Tour, provided that a measurement with an uncertainty at the signal level of k_2 can be obtained with another measurement technique, such as the assessment of surface deformations with a 6-degree-of-freedom sensor positioned on the surface (F. Bernauer et al. 2020; V. Filice et al. 2024). Specifically, with 4 hr Ka-band tracking time, two pictures per flyby, and 30 landmarks per picture, the rock-to-ice mass ratio can be constrained to 26% and the ice shell thickness to 15%.

We remind the reader that this is a particular discussion of the mission requirements pertaining to the $sh2/sh3$, k_2, ε, and gs parameter set. The results of a comprehensive sensitivity analysis are presented in Appendix B.

5. Conclusions

In this paper, we presented a new approach to fold science objectives at the earliest stages of mission design. By establishing a clear relationship between the required precision on the geodetic measurements and the scientific goals of the mission, such an approach would allow the mission designers to make essential, rapid, and informed adjustments without compromising scientific outcomes, both at the beginning and during the later stages of the mission's development. This "reverse mapping" approach is noteworthy for its originality and efficiency, which could potentially serve as a point of inspiration for other experiments in planetary science missions to pursue a similar approach. We employed this methodology to develop guidelines for the UOP gravity experiment designs, demonstrating how this inverse approach can facilitate the definition of measurement requirements subsequent to the identification of scientific objectives, but also rapidly assess the efficacy of geodetic measurements in constraining interior parameters.

Based on a series of truth interiors encompassing both ocean-bearing and oceanless models of the Uranian satellites, we assessed the expected uncertainties associated with key interior parameters (i.e., the ice shell and ocean thicknesses, and the rock-to-ice mass ratio) as a function of the uncertainties on key geodetic measurements (mean MoI, tidal Love number, diurnal libration amplitude, and obliquity). By conducting ~600 MCMC simulations for each truth model, we build comprehensive measurements-to-interior maps for each interior parameter. We used these "lookup tables" to determine the required geodetic measurement precisions needed to meet some of the UOP scientific objectives. These maps are provided to the scientific community as MRTs (see Appendix C).

Assuming that Ariel has a 20 km thick ocean, our results suggest that determining its rock-to-ice ratio with better than 5% accuracy requires measuring all four geodetic parameters (MoI, k_2, g_s, and ε) with 1% accuracy or better. Determining the ocean thickness presents an even more challenging task. In order to determine Ariel's ocean thickness with a 30% uncertainty level, the absolute precisions required on the MoI, k_2, g_s, and ε are 9.2×10^{-4}, 1.4×10^{-4}, 2.4×10^{-1} m, and 2.5×10^{-1} m, respectively. The ice shell thickness (d_s) is comparatively easier to constrain and can be determined with an uncertainty of 20%–30% by measuring the tidal Love number and/or libration amplitude at the signal level for all satellites. An enhancement in the determination of the libration amplitude enables a more precise estimation of the ice shell thickness for Ariel, Umbriel, Titania, and Oberon, whereas k_2 is the primary influencing factor for Miranda. The actual ocean thickness mainly affects the required precision to determine d_o itself. The thinner the ocean, the more precise the geodetic measurements must be to achieve a given level of uncertainty on d_o. The precisions on the determination of the ice shell thickness and the rock-to-ice ratio are less affected by the actual ocean thickness. Our study also demonstrated that a multitude of combinations for the measurement precision on MoI, k_2, g_s, and ε can be employed to determine an interior parameter with a desired uncertainty. Some combinations may be particularly advantageous for mission design, as they do not necessitate the measurement of all four geodetic observables with high precision. Relaxing the uncertainty requirement for one observable results in an increased precision requirement for the others. Some observables tend to compensate for each other, specifically g_s and k_2. When attempting to estimate several interior parameters simultaneously, such as d_o, rock-to-ice ratio, and d_s, it became evident that achieving precise measurements across all parameters is a particularly difficult endeavor. For instance, in the case of Titania, it is necessary to determine all four geodetic parameters with an uncertainty of 1% or less to determine the three interior parameters at the 30% level. It is unlikely that the three parameters can be measured to a 30% level with UOP, given the experience from the 10 Cassini flybys of Titan and the resulting level of precision on its geodetic parameters.

A covariance analysis was conducted to confirm the difficulty in constraining the interior parameters of the Uranian satellites. Specifically, we simulated Doppler and optical data from the UOP mission. Given the limited characterization of the gravity experiment design at this early stage of the mission, we analyzed two orbital tours, various measurement strategies, and inversion settings, resulting in approximately 15,000 simulations per moon. Our mapping technique enabled us to rapidly assess the performance of each of these POD simulations in constraining the interior parameters. The discussion focused on the observation strategies required to achieve the desired precision in geodetic measurements for Ariel's hydrosphere thickness, ocean detection, and other internal parameters. To illustrate, we discovered that the most challenging interior parameter to constrain is the ocean thickness d_o, where only a few of the tested solutions achieved a relative uncertainty better than 100%. However, the rock-to-ice ratio could be constrained with a relative uncertainty of approximately 28% using 6 hr of Ka-band tracking, four pictures per flyby, and 10 landmarks per picture with the Decadal Tour. Instead, the ice shell thickness d_s, being the most precisely determined interior parameter, can be constrained with a relative uncertainty of 16% when using four pictures per flyby, 10 landmarks per picture, and 6 hr of Ka-band tracking with the same orbital tour. Nevertheless, diversified flyby geometries, exemplified by the Alternative Tour, demonstrated comparable performance in constraining Ariel's interior properties, despite the reduction in the number of close passes. This is contingent on the k_2 Love number being measurable with other techniques. As has been demonstrated, the final design of the tour has a significant effect on the scientific return of the GS experiment. Consequently, it is essential to conduct a thorough evaluation of the future and necessary iterations of the UOP trajectory in order to ascertain their impact on the experiment's scientific return.

These findings highlight the intricate and challenging nature of the measurement requirements for accurately characterizing Ariel's interior structure. However, these are specific observation strategies that are contingent on particular assumptions, the relevance of which can shift during the course of mission development. A comprehensive sensitivity analysis is provided in Appendix B, in which the impact of several gravity experiments designed to study the interior of Ariel is assessed in terms of the geodetic parameter uncertainties, as well as in terms of interior parameters. Furthermore, the results of the aforementioned sensitivity analysis, as applied to the other Uranian satellites (namely Miranda, Umbriel, Titania, and Oberon), are also provided in Appendix B. We believe that these discussions will prove useful for mission designers.

Although the "lookup tables" have been developed for gravity experiments at the Uranian satellites, we wish to emphasize that this approach has the potential to be beneficial to a wider range of experiments and missions. Indeed, this approach enables the required precision for geodetic measurements to be determined in line with a given scientific objective, while also facilitating the rapid evaluation of the outcome of 1000 simulations in terms of the mission objectives, as demonstrated in this study.

Acknowledgments

V.F. was financially supported by the French Community of Belgium within the framework of the financing of an FRIA grant. V.F. extends its gratitude to Alfonso Caldiero for the fruitful discussions. R.-M.B. was financially supported by the Belgian PRODEX program managed by the European Space Agency in collaboration with the Belgian Federal Science Policy Office. The work by G.C. was supported by NASA under award No. 80GSFC21M0002. We thank Amy Simon and the UOP study team. We also thank Juan Arrieta, Martin Ozimek, Donald Ellison, Jacob Englander, Kyle Hughes, and Nobel Hatten for valuable trajectory design discussions.

Appendix A
Detailed POD Settings

A.1. Satellite Tours

Two different tours of the Uranian satellites are evaluated in this study, the Decadal Tour and the Alternative Tour. Their ground tracks are shown in Figures 6 and 8.

The Decadal Tour, as selected by the Planetary Science and Astrobiology Decadal Survey, is characterized by an initial inclined Uranus capture phase that enables the deployment of a probe designed to enter Uranus's atmosphere and relay scientific data to the orbiter. Thereafter, the spacecraft reaches a near-equatorial orbit that allows for a detailed science investigation of the five major moons. The equatorialization phase, which includes 15 resonant[6] flybys of Titania, and the subsequent nonresonant flybys of the other moons are designed to be nominally ballistic, meaning that no fuel is used. This tour is advantageous because it allows for targeting other moons through nonresonant transfers, as Uranus's major moons orbit near its equator. In this scenario, the spacecraft is planned to perform eight far nonresonant flybys of Umbriel, Oberon, and Ariel, followed by 11 close resonant flybys of Ariel to decrease the periapsis altitude relative to Uranus. The finale of this tour is characterized by a last maneuver that will dispose of the spacecraft into Uranus's atmosphere.

However, optimizing the required ΔV to reduce fuel consumption does not necessarily correlate with optimizing flybys for science objectives. Close (<3 body radii), slow (<$10\ \mathrm{km\ s^{-1}}$), and varied geometries are key to properly infer the geophysical characteristics of a body using radiometric data (see, e.g., Cassini at Titan; D. Durante et al. 2019). Due to the resonant orbits used, the Decadal Tour performs 12 and 14 close flybys of Ariel and Titania, respectively, all concentrated in the southern hemisphere with latitudes up to $-57°$ and $-87°$, respectively. The tour concludes with two close equatorial flybys of Oberon and only one far flyby of Miranda in the southeastern hemisphere. The use of resonance orbits limits not only the spatial sampling of the satellites but also the temporal sampling, which is necessary to determine signals at orbital frequencies, such as tides and librations. This temporal sampling is determined by the position of a satellite along its orbit, described by the value of its mean anomaly at the flyby epoch. The mean anomaly sampling of Ariel and Titania shown in Figure 9 is limited to [111°, 164°] and [117 °, 221°], respectively.

The Alternative Tour employs an equatorialization maneuver following the second post-capture apoapsis, rather than a resonance orbit with Titania (A. Simon, private communication). This necessitates nonresonant transfers between the satellites from the initial phase of the mission, as the spacecraft rapidly aligns with Uranus's equatorial plane. As a consequence, the number of flybys of Ariel and Titania is reduced, while the global coverage of the five moons is enhanced with at least two close flybys per satellite. Additionally, the ground track geometries of Ariel are more diversified, allowing for better overall coverage of the satellites with low- and high-latitude flybys. In contrast, the situation is reversed for Titania and Oberon, with high-latitude flybys being replaced by equatorial flybys for Titania and vice versa for Oberon. The C/A distances and relative velocities of the best flybys for each moon are comparable between the two tours, namely C/A distances of less than a body radius and relative velocities of approximately $5\ \mathrm{km\ s^{-1}}$. The Alternative Tour demonstrates improved mean anomaly sampling, particularly for Ariel and Titania, with flybys occurring at 198°.55, 199°.92, 218°.55, 349°.04, and 352°.00 for the former and 106°.41, 134°.58, 183°.57, 197°.01, and 317°.49 for the latter. This allows a better temporal sampling of the libration and tidal signals (see Figure 9).

[6] Two bodies are in orbital resonance if their orbital periods can be expressed as a ratio of two integers.

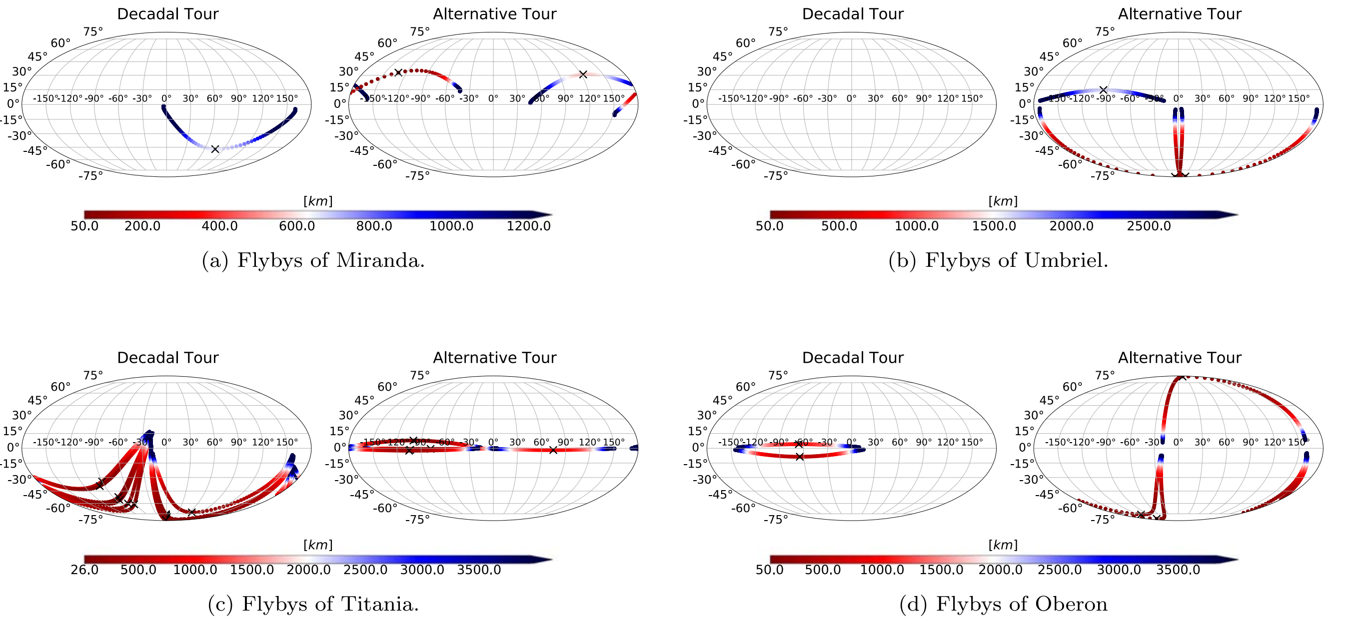

(a) Flybys of Miranda.

(b) Flybys of Umbriel.

(c) Flybys of Titania.

(d) Flybys of Oberon

Figure 8. UOP ground tracks (±30 minutes around C/A) with respect to the Uranian satellites. Ariel's flybys are shown in Figure 6. Colors show the altitude with respect to the moons' surface, whereas the crosses show the point of C/A. Only flybys with a C/A distance less than three body radii are shown.

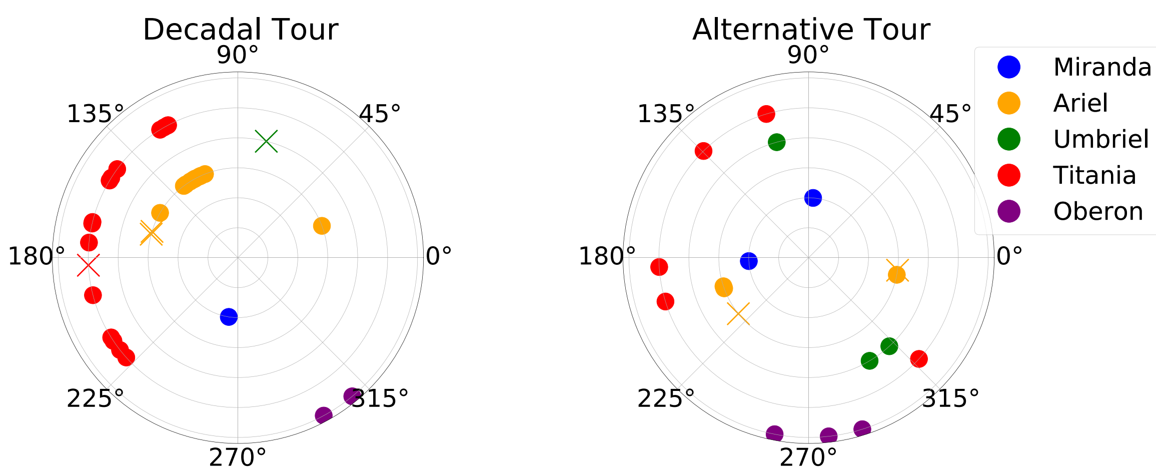

Figure 9. Orbital mean anomalies of the Uranian satellites at UOP C/A epochs. Circles are for flybys with closest distances less than three body radii, *x* otherwise.

A.2. Simulated Measurements

The UOP spacecraft will be equipped with an HGA and potentially an USO that will allow the establishment of a two/three-way coherent link with NASA's Deep Space Network (DSN) ground stations to support telemetry, tracking, and command activities. As with many past planetary missions, the telecommunication subsystem can be used to perform GS experiments by collecting Doppler measurements (e.g., S. W. Asmar et al. 2017). The precision of radiometric measurement depends primarily on propagation noise, including plasma and Earth troposphere noises, as well as thermal and mechanical noises from both ground-based and onboard spacecraft instrumentation, rather than on the performance of the onboard coherent transponder. Ka band (32.5–34.0 GHz) is less susceptible to plasma effects than X band (7.2–8.4 GHz), making it preferable for scientific measurements. Nevertheless, a dual-link configuration can effectively reduce the impact of charged particle noise by approximately 75% during superior solar conjunctions, provided that spacecraft tracking is required during this period (B. Bertotti et al. 1993). The wet component of the troposphere can be calibrated up to 70% using one or multiple Advanced Water Vapor Radiometers (AWVRs; D. R. Buccino et al. 2021). At present, only the DSS-25 antenna in the DSN Goldstone complex is equipped with a Ka-band uplink and an AWVR. By the beginning of the UOP science phase (early 2050s), the Canberra and Madrid complexes are expected to also be equipped with at least one ground station with the same capabilities as Goldstone's.

The notional payload of UOP also includes an NAC and a WAC that can be used for optical navigation. The latest developments in space image systems involve the use of gimbals for precise pointing and enhanced pixel resolution to obtain high-resolution imaging data for measuring a target's geophysical and geodetic properties. For instance, the Advanced Pointing Imaging Camera concept (R. S. Park et al. 2020) provides a system that comprises an NAC with a pixel resolution of 18 μrad and 4° field of view. Additionally, the system is equipped with a WAC that has a pixel resolution of 82 μrad and 18° field of view. The combination of these two

Table 6
Dynamical Model Parameters for the Uranian Satellites

	J_2	k_2	α_{2050} (deg)	δ_{2050} (deg)	W_0 (deg)	$\dot{W}$ (deg day^{-1})	g_s (deg)	M_0 (deg)	$\dot{M}$ (deg day^{-1})
Miranda	6.74E–03	1.48E–03	78.2590	19.5040	148.70	254.69	−1.27E–02	72.37	254.64
Ariel	1.30E–03	1.56E–02	77.3177	15.1278	23.09	142.84	−2.66E–03	119.76	142.82
Umbriel	4.88E–04	1.55E–02	77.3711	15.1200	71.26	86.87	−3.15E–03	258.30	86.86
Titania	1.01E–04	3.29E–02	77.3605	15.1450	101.58	41.35	−2.16E–04	53.20	41.35
Oberon	4.20E–05	3.15E–02	77.3222	14.8438	172.57	26.74	−1.03E–04	139.73	26.74

Note. The reference epoch of α_{2050} and δ_{2050} is the mission epoch (2050 January 1 12:00:00 UTC). The reference epoch for W_0 and M_0 is J2000.

cameras, in conjunction with the presence of two gimbals, enables the instrument to be pointed with a pointing accuracy of 2″, without the need to change the attitude of the spacecraft. Other imaging systems that have flown, such as the Long Range Reconnaissance Imager on the New Horizons mission (M. W. Noble et al. 2009), or that will fly, such as the Europa Imaging System on Europa Clipper (R. T. Pappalardo et al. 2024), provide similar performance characteristics.

The NASA-JPL orbit determination software MONTE (S. Evans et al. 2018) is used to simulate Doppler and optical data with noise levels that reflect the current state of the art. Specifically, synthetic Doppler data are computed for a coherent two/three-way direct-to-Earth link, with a noise level of 0.1 mm s^{-1} and 10 μm s^{-1} for X/X and Ka/Ka, respectively, at a 60 s integration time (S. W. Asmar et al. 2005). In order to extensively characterize the possible GS experiment, we test independently the X- and Ka-band performances, as well as different tracking times (from 1 to 6 hr around C/A). As is done for radiometric data, optical data are also simulated with a state-of-the-art noise level of 2″. The impact of the number of landmarks observed per image (5, 10, 30, and 50) and the impact of the number of images per flyby (2, 4, 6, and 8) are investigated.

A.3. Dynamical Models

The spacecraft trajectory is mainly driven by the gravity field of Uranus and is perturbed by the gravity fields of the Sun, the other planets, and the satellites during the flybys. For our modeling, we use the zonal field of Uranus and body frame (BF) orientation of R. A. Jacobson (2014, Table 12) and the orbit of the Uranian satellites as defined by JPL's Uranian satellite ephemeris file URA111.[7] We account for the point-mass gravity of the Sun and planets. Nongravitational forces also perturb the spacecraft motion. We consider the SRP acting on a sphere that encompasses the maximum dimension of the UOP spacecraft.

The external gravity potential of the satellites is classically modeled using a spherical harmonic expansion (W. M. Kaula 1966):

$$U(r, \lambda, \phi) = \frac{GM}{r}\sum_{n=0}^{\infty}\sum_{m=0}^{n}\left(\frac{R}{r}\right)^n \bar{P}_{nm}(\sin\phi) \times [\bar{C}_{nm}\cos(m\lambda) + \bar{S}_{nm}\sin(m\lambda)], \quad \text{(A1)}$$

where r is the radial distance, ϕ the latitude, and λ the longitude of the spacecraft in the BF of the moon; G is the gravitational constant; M is the mass of the body and R the reference radius of the expansion; $\bar{C}_{nm}$ and $\bar{S}_{nm}$ are the fully normalized spherical harmonic coefficients of degree n and order m; and $\bar{P}_{nm}$ are the fully normalized (4π normalization) associated Legendre functions. The fully normalized zonal harmonic coefficients are defined as $\bar{J}_n = -\bar{C}_{n0}$. The unnormalized second-degree coefficients (J_2 and C_{22}) are computed for a three-layer model with an ocean of 20 km assuming hydrostatic equilibrium and by inverting Radau Equation (1) (see Table 6). The higher-degree coefficients (up to degree 10) are computed following the method of G. Cascioli et al. (2024, and references therein). In this method, a set of spherical harmonic coefficients is generated to simulate a three-layer body consisting of a rocky core, a global liquid layer, and an ice shell. The seafloor and ice shell topography are generated using a power law to define their random spectrum (after the assigned layer thicknesses are set), specifically $P_l = k/l^{\beta}$, where P is the power spectrum, l is the degree, and k and β are prescribed coefficients. The resulting topography coefficients are then converted to gravity coefficients using Equations (3a)–(3b) of G. Cascioli et al. (2024). It is assumed that there is no compensation of the seafloor.

Periodic changes in the potential, as reflected in changes to the normalized spherical harmonic coefficients, i.e., $\Delta\bar{C}_{nm}$ and $\Delta\bar{S}_{nm}$, due to gravitational tides can be written as (e.g., as used by the International Earth Rotation and Reference Systems Service; R. Eanes et al. 1983; D. D. McCarthy & G. Petit 2003)

$$\Delta\bar{C}_{nm} - i\Delta\bar{S}_{nm} = \frac{k_{nm}}{2n+1}\frac{M_j}{M}\left(\frac{R}{r_j}\right)^{n+1}\bar{P}_{nm}(\sin\phi_j)e^{-im\lambda_j}, \quad \text{(A2)}$$

where k_{nm} represents gravitational Love numbers of degree n and order m, M_j represents the mass of the primary, r_j represents the distance of the body from the primary, and λ_j and ϕ_j represent body-fixed longitude and latitude of the primary, respectively. We set $k_{2m} = k_2$ because achieving the minimum spatial and temporal coverage required to measure better than the global average of the second-degree gravitational tide with only a few flybys per satellite is too challenging (see, e.g., P. Cappuccio et al. 2020). Moreover, we compute the Love number with the method of R. Sabadini et al. (2016) assuming a spherical body, for which the Love numbers are degenerate with respect to m ($k_{20} = k_{21} = k_{22}$; A. I. Ermakov et al. 2021). The k_2 values are computed for a three-layer model with an ocean thickness of 20 km (see Table 6).

The orientation of a satellite's BF is defined by the R.A. (α) and decl. (δ) of its spin axis and by the prime meridian location

[7] https://naif.jpl.nasa.gov/pub/naif/generic_kernels/spk/satellites/ura111.bsp

(W) with respect to the International Celestial Reference Frame (ICRF J2000). The current IAU recommendations (B. A. Archinal et al. 2018) for the Uranian satellites are based on outdated ephemerides and neglect libration and obliquity. Here we use an orientation model that is consistent with the URA111 ephemeris and that includes the libration and obliquity as modeled in R.-M. Baland et al. (2025). This is essential for our study, since we need an orientation model that is consistent with the ephemerides we use and since the satellite orientation parameters are estimated parameters. The three angles are defined as follows:

$$\alpha(t) = \alpha_{2050} \tag{A3}$$

$$\delta(t) = \delta_{2050} \tag{A4}$$

$$W(t) = W_0 + \dot{W}t + g_s \sin(M_0 + \dot{M}t). \tag{A5}$$

Since the obliquity of Uranus's largest satellites varies over longer periods than those of the UOP space mission (R.-M. Baland et al. 2025), we set α and δ to their values at 2050, a date representative of the mission period; see Table 6. The epoch rotation angle W_0 is set at J2000. $\dot{W}$ is the rotation rate, and g_s is the amplitude of the diurnal libration. $M = M_0 + \dot{M}t$ is the mean anomaly, with t the time from J2000 and $\dot{M}$ the time derivative of M.

A.4. Estimated Parameters

The Doppler and optical data for each flyby are simulated and processed with a multiarc approach (A. Milani & G. Gronchi 2009) in order to determine the expected uncertainties (1σ formal errors) of the estimated parameters in our POD solution. This approach enables the inherent errors of the dynamical model, numerical rounding errors of the orbit propagators, and orbit maneuvers to be effectively absorbed by localizing errors to their respective intervals. This is accomplished in practice by separation of dynamical parameters into local (e.g., spacecraft initial state) and global parameters (e.g., gravity coefficients).

The estimated parameters and the associated a priori uncertainties used for the UOP GS experiment simulations are presented in Table 7. It should be noted that the set of estimated parameters varies because some parameters are sometimes kept fixed, when preliminary results show no sensitivity to them, as we discuss in Section 4.2. The estimated parameter set, however, always includes the spacecraft state (one per flyby), the satellite GM, a minimal combination of gravity coefficients (J_2 and C_{22}; see below), and one SRP scaling factor per arc. If optical data are simulated, the base set is completed by the camera pointing errors along the camera frame axes and by the landmarks' position (latitude, longitude, and radial coordinates for each landmark).

Different combinations of the maximum degree (n) and order (m) of the estimated gravity static coefficients are tested, beginning with only the degree-2 coefficients J_2 and C_{22} up to a maximum full degree and order (3 for Miranda, Ariel, and Umbriel; 4 for Ariel and Titania). The impact of applying a hydrostatic constraint ($J_2/C_{22} = 10/3$) on the estimated formal errors is also evaluated. When the satellite BF orientation with respect to ICRF is estimated (parameters: α, δ, $\dot{W}$), the coefficients C_{21}, S_{21}, and S_{22} are not estimated and are set to 0. These coefficients are instead estimated when the frame is fixed. The term “quadrupole” is employed when only J_2 and C_{22} gravity coefficients are estimated. The tidal Love number k_2 is estimated through temporal variations in J_2, C_{22}, and S_{22}. The uncertainty in the obliquity is derived from the uncertainties in the determination of the spin axis R.A. α and decl. δ from the spherical trigonometric relation $\cos\varepsilon = \sin\delta\cos J - \cos\delta\sin J\sin(\alpha - N)$. J and N are respectively the orbital inclination and ascending node longitude of the satellite with respect to ICRF J2000. The libration amplitude g_s is estimated only if the frame is estimated.

Table 7
Estimated Parameters and Associated A Priori Uncertainties

Parameter	Type	A Priori Uncertainty
UOP state	Local	1 km, 1 m s^{-1}
SRP scaling factor	Local	0.25
Camera pointing	Global	$2''$
Landmark position	Global	Unconstrained
GM	Global	Unconstrained
$C_{l,m}$, $S_{l,m}$	Global	Unconstrained
α	Global	Unconstrained
δ	Global	Unconstrained
$\dot{W}$	Global	Unconstrained
k_2	Global	Unconstrained
g_s	Global	Unconstrained

Appendix B
Impact of Measurement Strategies and Parameter Estimates

Given the early stage of the UOP mission, many different design choices are not finalized yet. This includes the type of radiometric subsystem, the trajectory, and the instrumentation on board the spacecraft. For this reason, we explored a wide number of combinations of these assumptions to better understand their effect on the retrieved geophysical observables' uncertainty (see Appendix A for a detailed description). The objective is to characterize the general trend with respect to flyby geometries, measurement strategies, and parameter set. It should be noted that the selection of the final parameter set is entirely data dependent, a known principle within the GS community. The optimal parameter set is the one that yields the best fit to the data and thus cannot be selected in advance. The aim of testing all these parameter sets is to assess the impact of correlations and identify observation settings that can mitigate them.

We provide a qualitative discussion of expected uncertainties of the MoI (Figure 10), the k_2 Love number (Figure 11), the libration amplitude g_s (Figure 12), and obliquity (Figure 13) across all solutions obtained from our covariance analysis investigation for Ariel. As previously stated in Section 4.2.2, only solutions where the values of σ_{MoI}, σ_{k_2}, σ_{g_s}, and σ_ε are equal to or below the nominal values are shown. As anticipated, optical data are essential for determining the libration amplitude (g_s) and obliquity (ε) to the level indicated in Table 1 (see Figures 12 and 13). Generally speaking, the Decadal Tour leads to better performance in determining the MoI and k_2 thanks to the higher number of flybys and therefore the additional number of measurements. The supplementary Doppler data allow the determination of Ariel's gravity field up to degree and order 4×4, whereas the Alternative Tour yields the determination only up to degree and order 3×3 (see Figure 14). The enhanced resolution of the gravity field results in a reduction in the correlation between the higher-degree and order gravity coefficients and the MoI/k_2. This is evidenced by the reduced impact on the formal error when higher degrees and orders are estimated (see Figures 10 and 11, bottom panels).

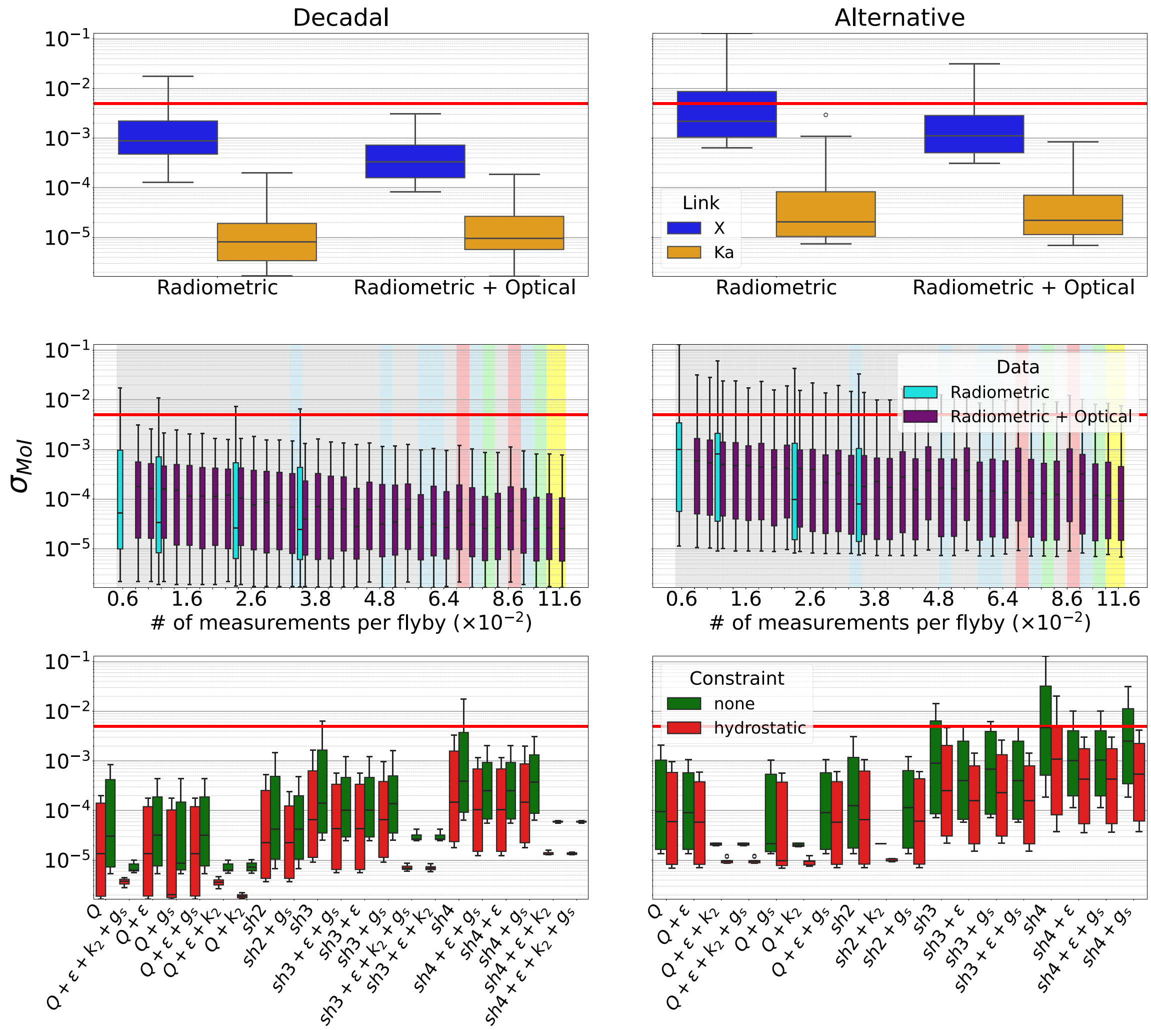

Figure 10. Computed formal errors of Ariel's MoI. The box-and-whisker plot illustrates the conventional statistical measures: the lower boundary of the box represents the 25th percentile, the upper boundary the 75th percentile, and the line within the box the 50th percentile. The lower whiskers extend to a value that is 1.5 times below the 25th percentile, while the upper whiskers extend to a value that is 1.5 times above the 75th percentile. Circles represent data points that fall outside the range of the whiskers. Symbols are used to define the parameter sets. Specifically, the letter Q stands for "quadrupole," whereas shN means that all gravity coefficients up to maximum degree and order $N \times N$ are estimated. The number of simulated measurements per flyby is equal to $2N_{\mathrm{pictures}}{}^{*}N_{\mathrm{landmarks}} + N_{\mathrm{Doppler}}$. Given that the incremental step is not constant, colored areas are used to define the step (gray: 0.2; blue: 0.4; orange: 0.6; green: 0.8; yellow: 1.2). The red solid lines represent the target uncertainty (0.005), as outlined in Table 1. The results of the sensitivity analysis for the remaining Uranian satellites are presented in a figure set in the online journal.

(The complete figure set (4 images) is available in the online article.)

The results on MoI and k_2 also highlight the importance of the optical data for these gravity parameters. It should be noted that the degree-two coefficients C_{21}, S_{21}, and S_{22} are fitted when the rotation body-fixed frame is not estimated, as explained in Appendix A.4. Indeed, there is an implicit (and indirect) relationship between the gravity field and the (unknown) rotation frame that has a notable influence on the determination of MoI and k_2, due to correlation effects. As a result, the determination of MoI and k_2 is more accurate when the frame is also estimated and well resolved through optical measurements (see Figures 10 and 11, bottom panels). However, this trade-off is not straightforward because the enhanced data set (radio + optical) introduces not only additional sensitivity but also an overall uncertainty due to imperfect a priori knowledge of the landmark positions.

Variate and complementary flyby geometries have a strong impact on the determination of the geodetic parameters since they yield to complementary measurements. This is straightforward when examining the uncertainty of the rotation parameters, which is constantly lower for the Alternative Tour, but also for MoI and k_2 we see comparable uncertainties. In fact, despite the reduced number of flybys (and, consequently, of measurements), this tour exhibits a more comprehensive temporal and spatial coverage (see Figure 8 and Appendix A.1), which enables the reduction of parameter correlations as shown, for a specific case, in Figure 15.

Although the maximum resolvable degree is 3 or 4 (see the sensitivity analysis presented in Figure 14), we now examine the impact of estimating higher degrees and orders (up to 6×6) of the gravity coefficients in terms of scientific requirements. We see from Figure 14 that in such a case the power spectrum of the degree-2 formal errors is degraded by up to one order of magnitude for the Alternative Tour and by less than a factor of 2 for the Decadal Tour. For both tours, degree-2 estimated sigmas remain lower than ~1% of the truth if a 6×6 gravity field is estimated, still satisfying the MoI precision

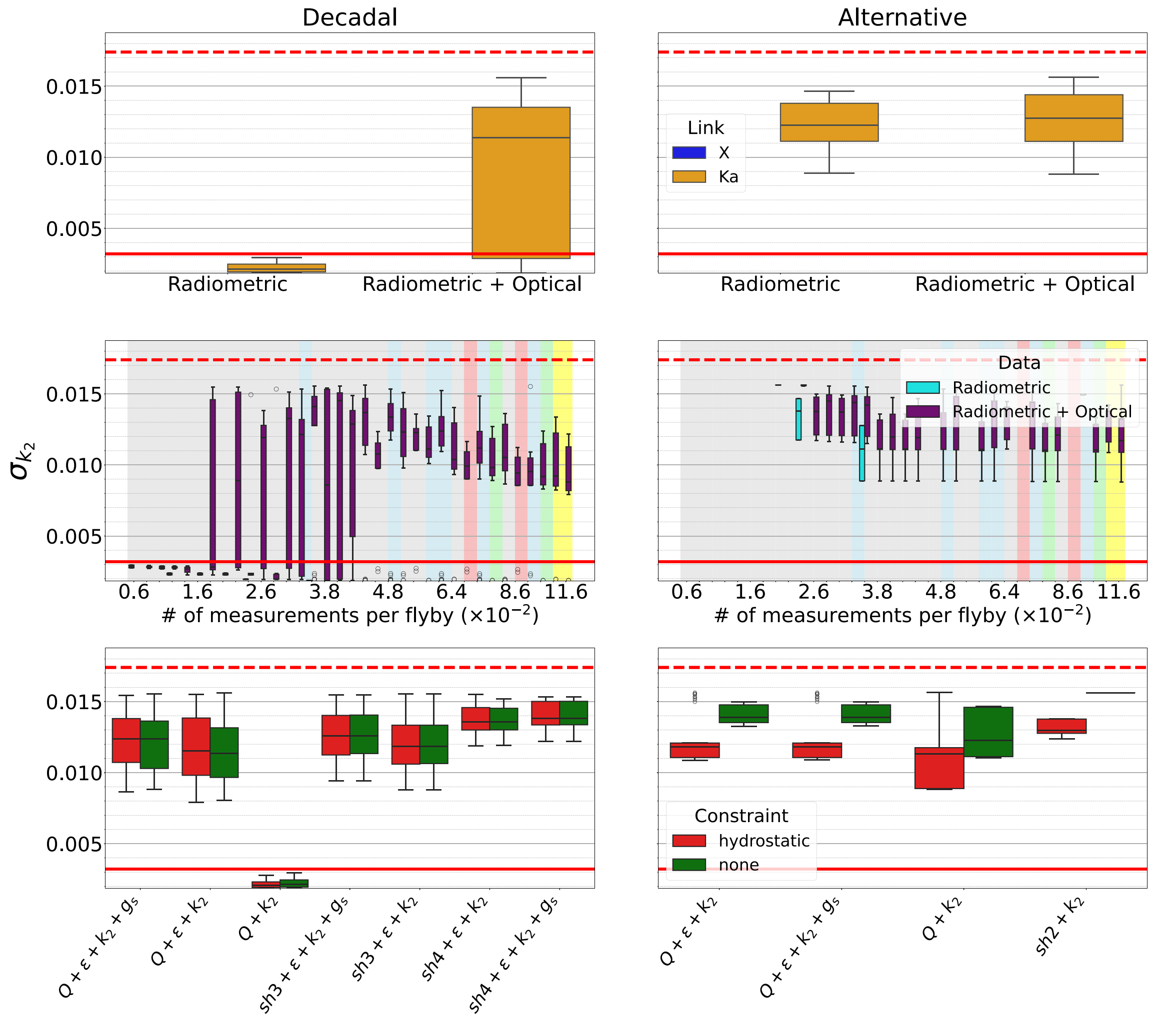

Figure 11. Computed formal errors of Ariel's Love number (k_2). A detailed explanation of the figure can be found in Figure 10. The red dashed line is the optimistic requirement for ocean detection (0.0174), and the red solid line is the requirement to detect differentiation (0.0032; see Table 1). The results of the sensitivity analysis for the remaining Uranian satellites are presented in a figure set in the online journal.

(The complete figure set (4 images) is available in the online article.)

requirement of 0.005 (Figure 16). The repetitive, equatorial flybys of the Decadal Tour are favorable to the estimation of k_2 as evidenced by the literature (see, e.g., R. S. Park et al. 2011). This is corroborated by the limited degradation of σ_{k_2} with the increasing maximum degree considered (see Figure 16).

We also quantify the impact of the assumptions we made regarding Uranus gravity and the moon ephemerides, both of which were considered well-known in our simulations. We see in Figure 16 that the Uranus gravity field has a minor effect on our results while fitting the moon ephemerides with the other parameters degrades the estimated precisions by a factor of about 2, which does not alter our conclusions.

The “reverse mapping” method enables direct discussion of the performance of a GS experiment design in terms of the internal parameters, as previously mentioned in Section 3 and illustrated in Figures 17, 18, and 19 for the ocean thickness, rock-to-ice ratio, and ice shell thickness, respectively. In order to correctly interpolate from the aforementioned “lookup table,” we assume an uncertainty at the signal level for the nonestimated parameters. This objective can be achieved through the implementation of alternative measurement techniques, such as the determination of k_2 through the assessment of surface deformations with a 6-degree-of-freedom sensor positioned on the surface, as suggested in Section 4.2.2, or through the measurement of the libration amplitude derived from the analysis of the body's orbital evolution, as illustrated by V. Lainey et al. (2024). It is acknowledged that this is a significant assumption with regard to the evaluation of the GS experiment design. However, the objective of this investigation is to explore trends as a function of the experiment design, rather than to provide final recommendations. As previously discussed, the same general trends are evident in this case for the geodetic parameters. The combination of radiometric and optical data enables a more precise estimation of the ocean and ice shell thickness, despite the absence of a solution that can accurately determine d_o. The Decadal Tour exhibits a distinct outlier, represented by an optimistic filtering strategy ($Q + k_2$) that proposes a relative uncertainty of 55%. It is evident that combining multiple precise measurements is necessary to properly constrain the interior parameter, as illustrated in the bottom panels of Figures 17, 18, and 19. The determination of the rock-to-ice mass ratio is overall constrained by the necessity of accurately determining the layer densities, which represents a particularly challenging task.

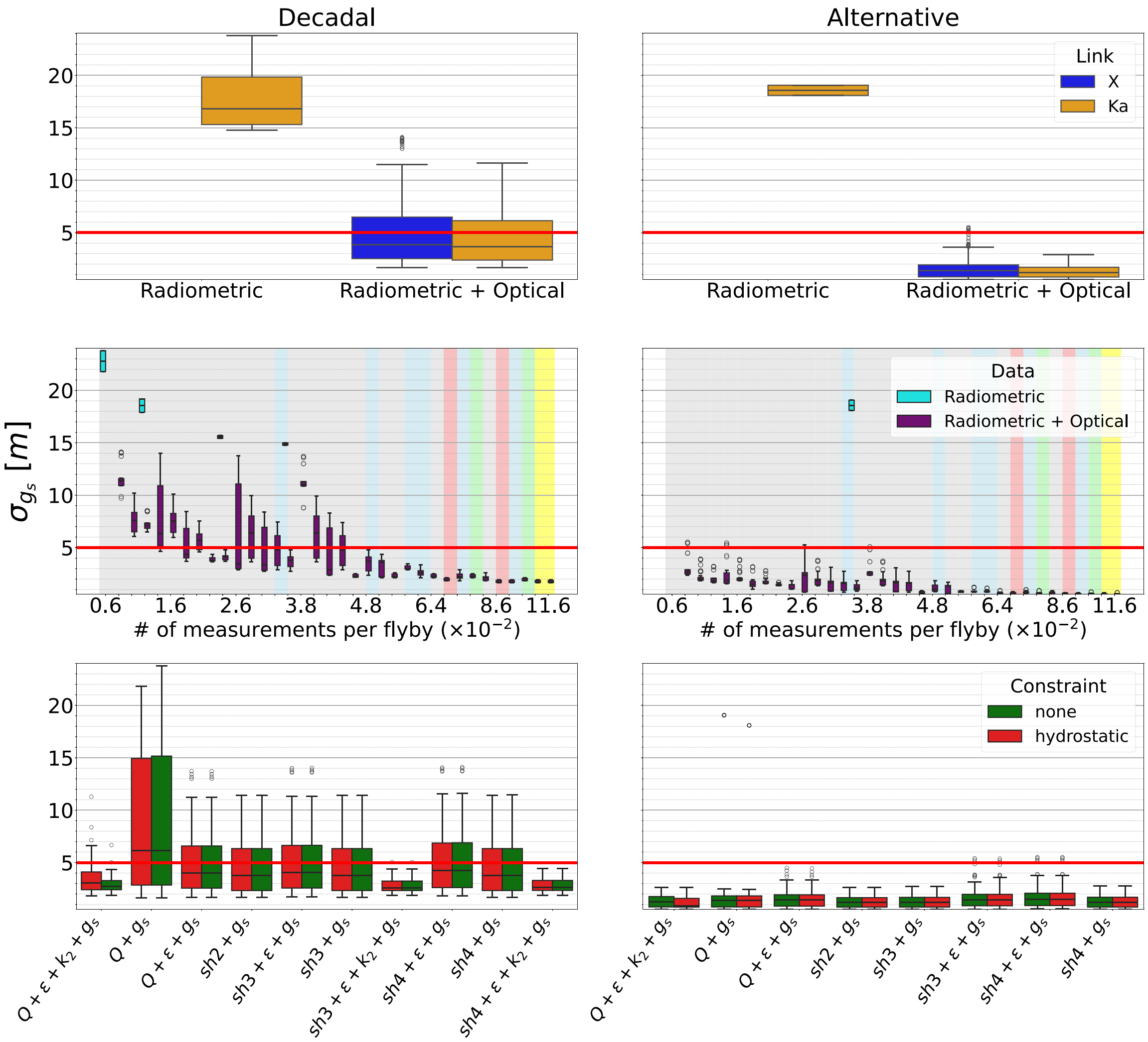

Figure 12. Computed formal errors of Ariel's libration amplitude (g_s). A detailed explanation of the figure can be found in Figure 10. The red solid line represents the target uncertainty (5 m), as outlined in Table 1. The results of the sensitivity analysis for the remaining Uranian satellites are presented in a figure set in the online journal.

(The complete figure set (4 images) is available in the online article.)

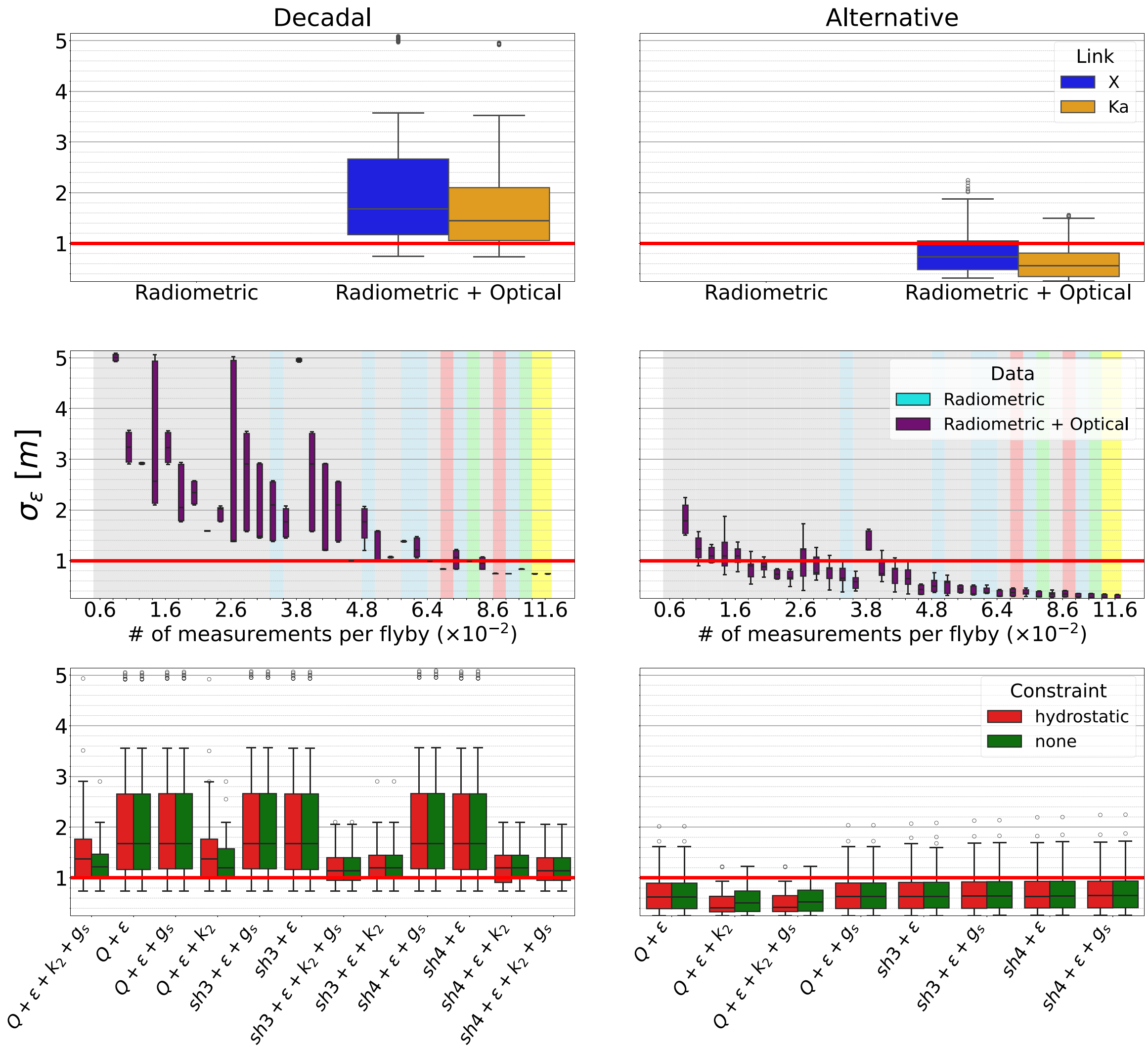

Figure 13. Computed formal errors of Ariel's obliquity (ε). A detailed explanation of the figure can be found in Figure 10. The red solid line represents the target uncertainty (1 m), as outlined in Table 1. The results of the sensitivity analysis for the remaining Uranian satellites are presented in a figure set in the online journal. (The complete figure set (4 images) is available in the online article.)

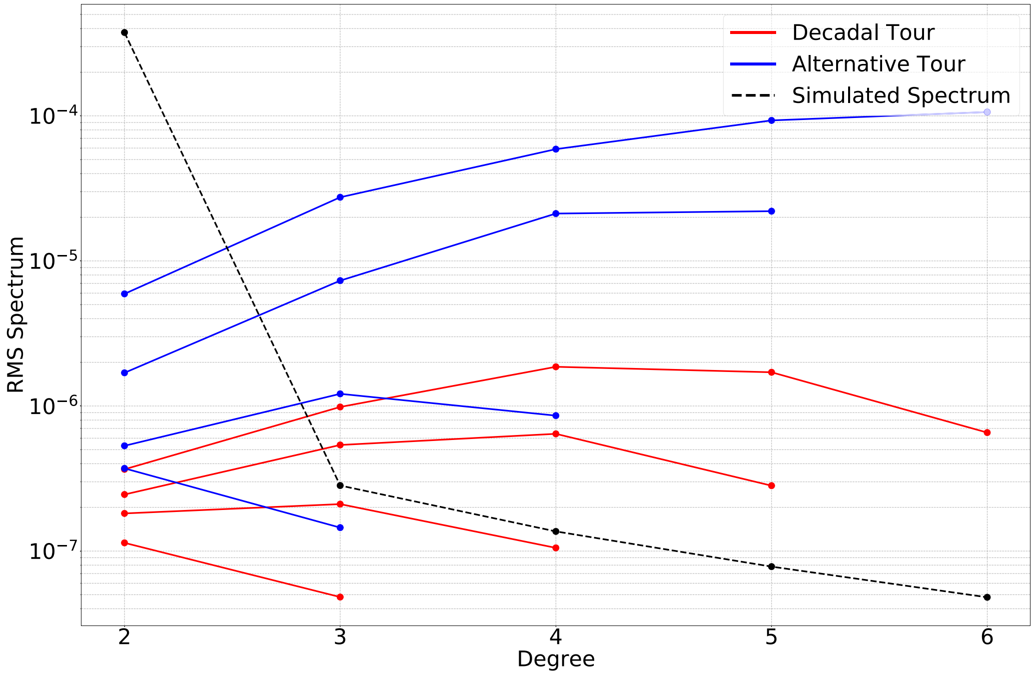

Figure 14. Ariel's rms gravity and error spectra expected from the GS experiment with the Decadal and Alternative Tour trajectories and nominal observation strategy (4 hr of tracking time centered on the C/A, Ka-band radiometric data, and optical data comprising four pictures per flyby with 10 landmarks per picture). The simulated gravity field (black dashed line) is computed in accordance with the methodology outlined in Appendix A.3.

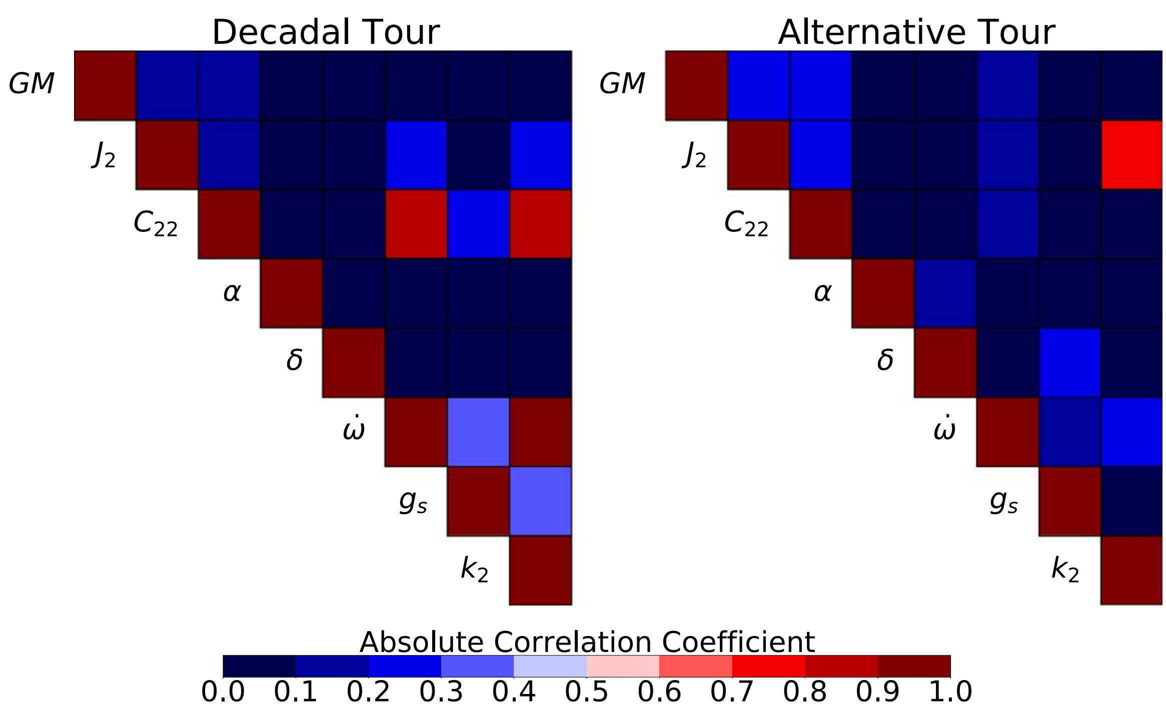

Figure 15. Correlation matrices of the POD solutions using the decadal and alternative tours for the parameter set $Q + \varepsilon + k_2 + g_s$. The measurement settings are characterized by the following: Ka band and 4 hr tracking time, four pictures per flyby, with 10 landmarks per picture. The hydrostatic constraint is not applied to the presented cases.

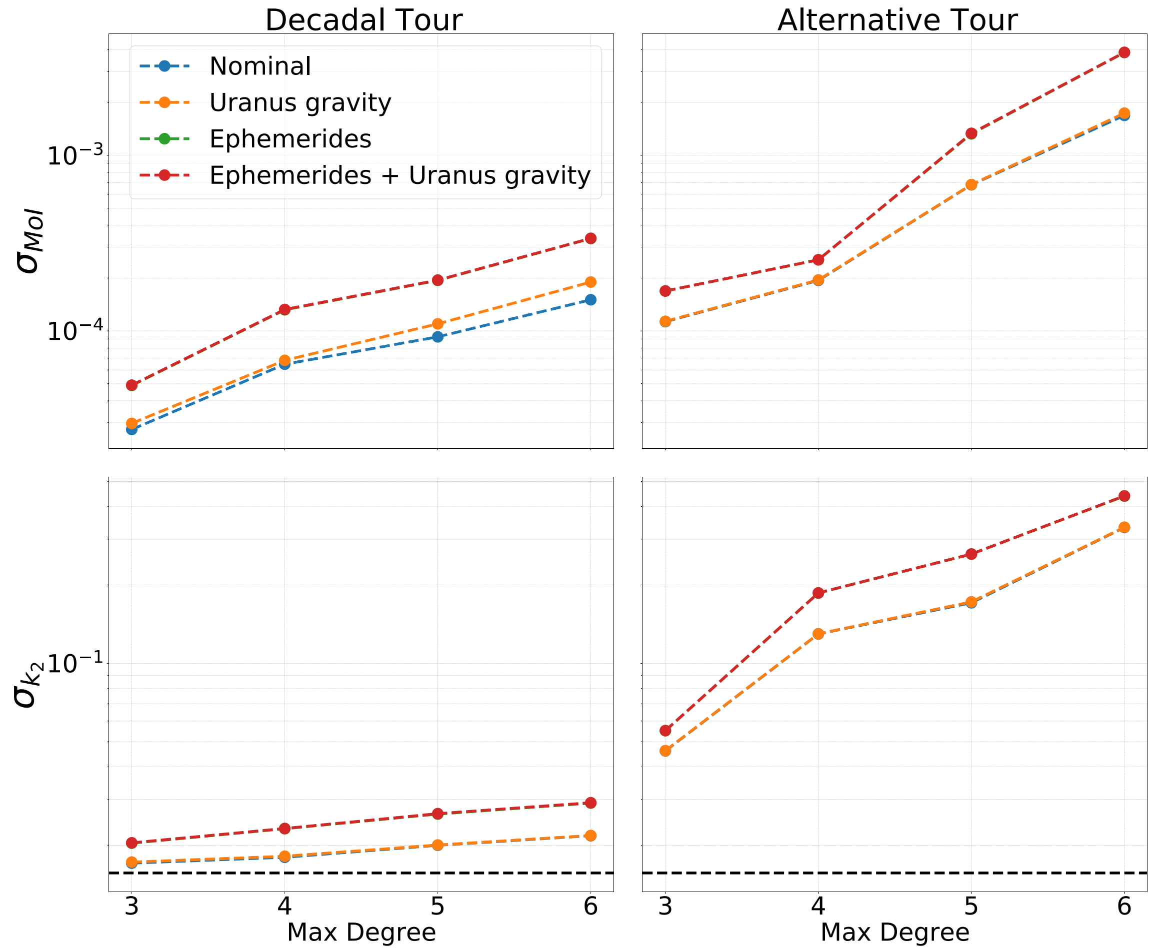

Figure 16. Ariel's expected uncertainty on the MoI and k_2 Love number as a function of the maximum estimated degree and order gravity field. The observation settings are the same as those of Figure 14. The effects of Ariel's position and/or Uranus gravity errors on the geodetic parameters of interest are tested. The black dashed line in the k_2 panels represents the true value of Ariel's Love number. Ariel's position is here fitted with an a priori uncertainty of 500 m along the three Cartesian coordinates ("Ephemerides case"). The influence of the errors of Uranus gravity is modeled by assuming an a priori of 30% of the current uncertainty estimates on GM, J_2, and J_4.

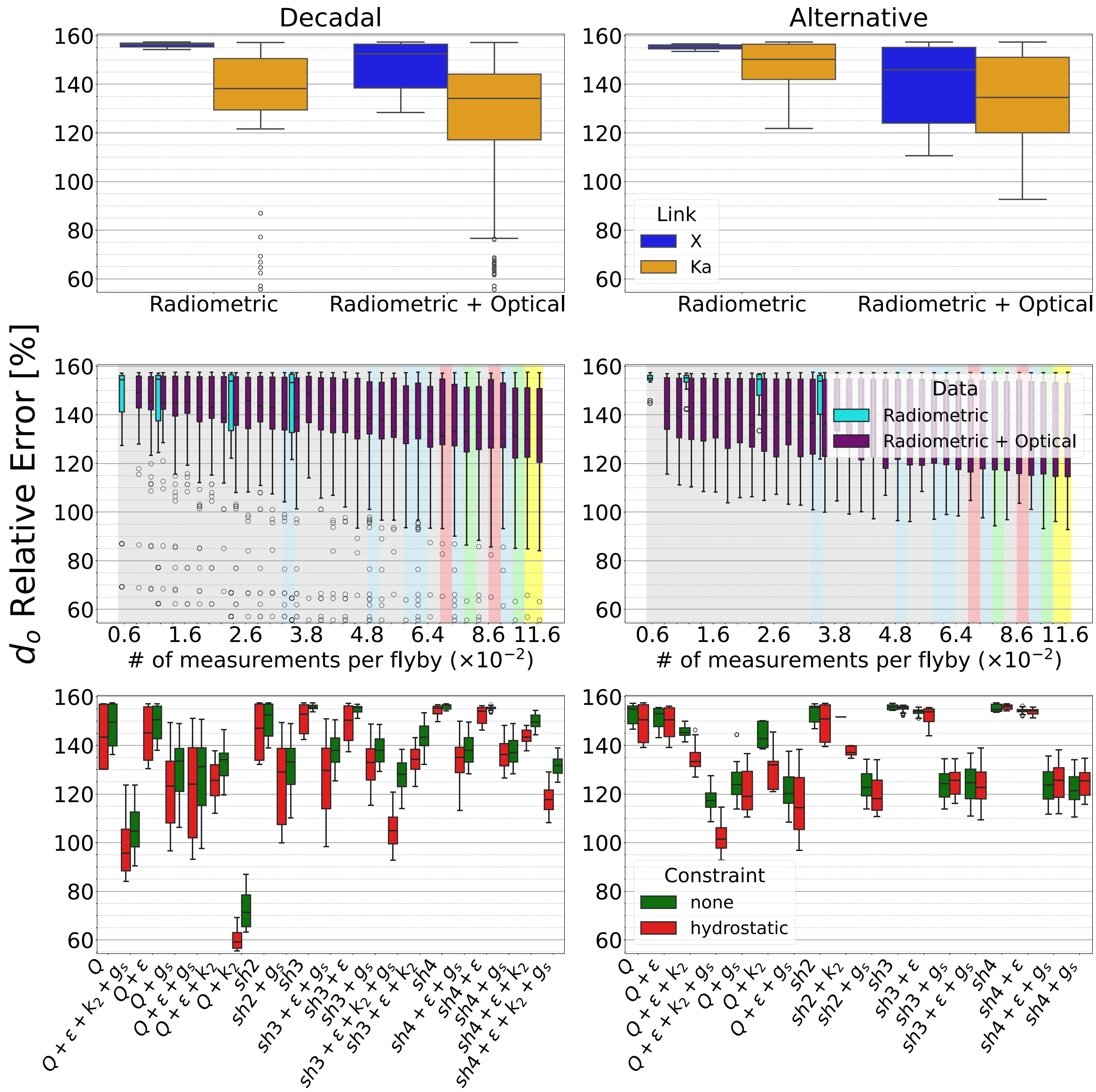

Figure 17. Interpolated uncertainty of Ariel's ocean thickness (d_o). A detailed explanation of the figure can be found in Figure 10. The results of the sensitivity analysis for the remaining Uranian satellites are presented in a figure set in the online journal.

(The complete figure set (4 images) is available in the online article.)

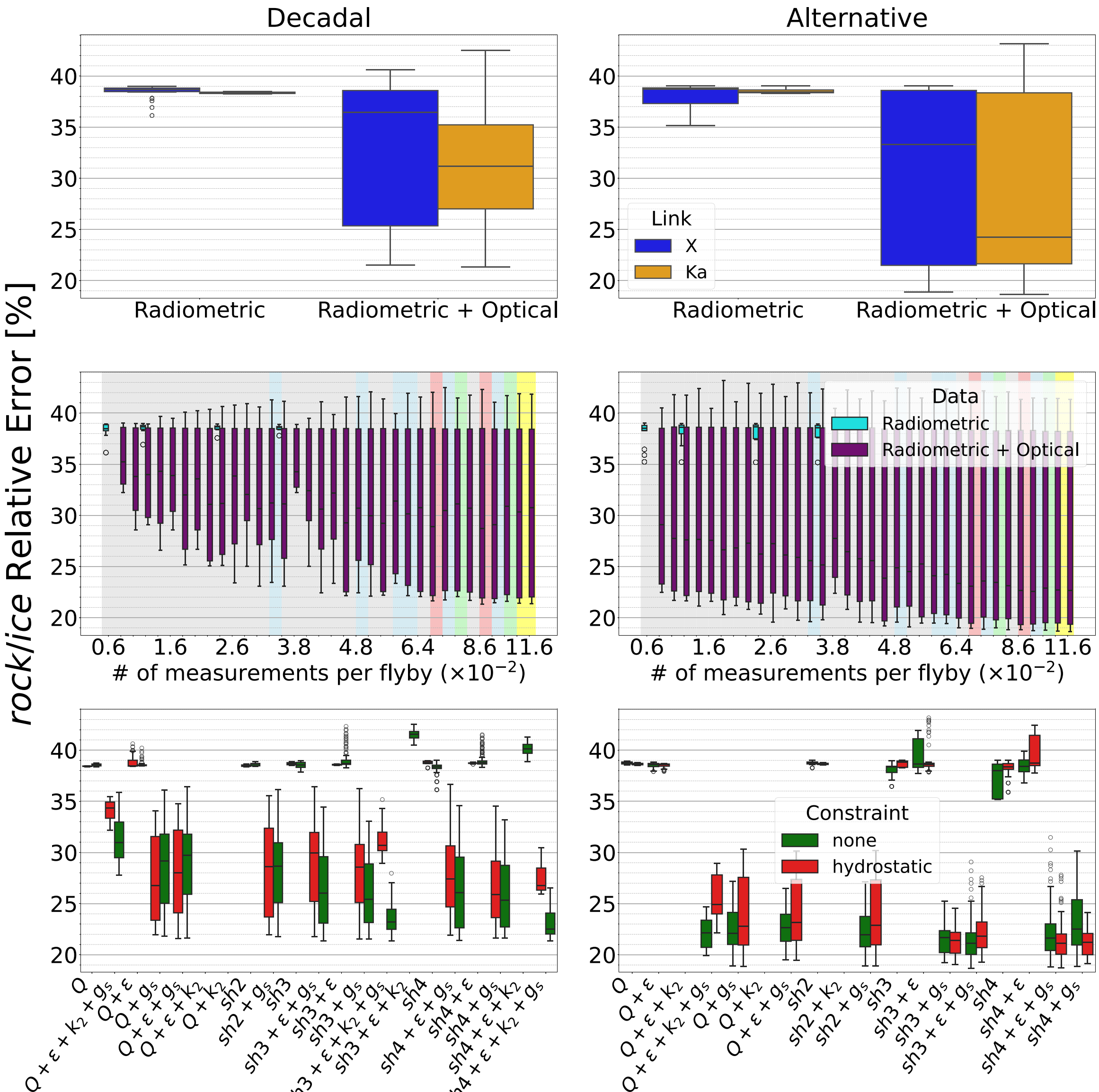

Figure 18. Interpolated uncertainty of Ariel's rock-to-ice ratio. A detailed explanation of the figure can be found in Figure 10. The results of the sensitivity analysis for the remaining Uranian satellites are presented in a figure set in the online journal.

(The complete figure set (4 images) is available in the online article.)

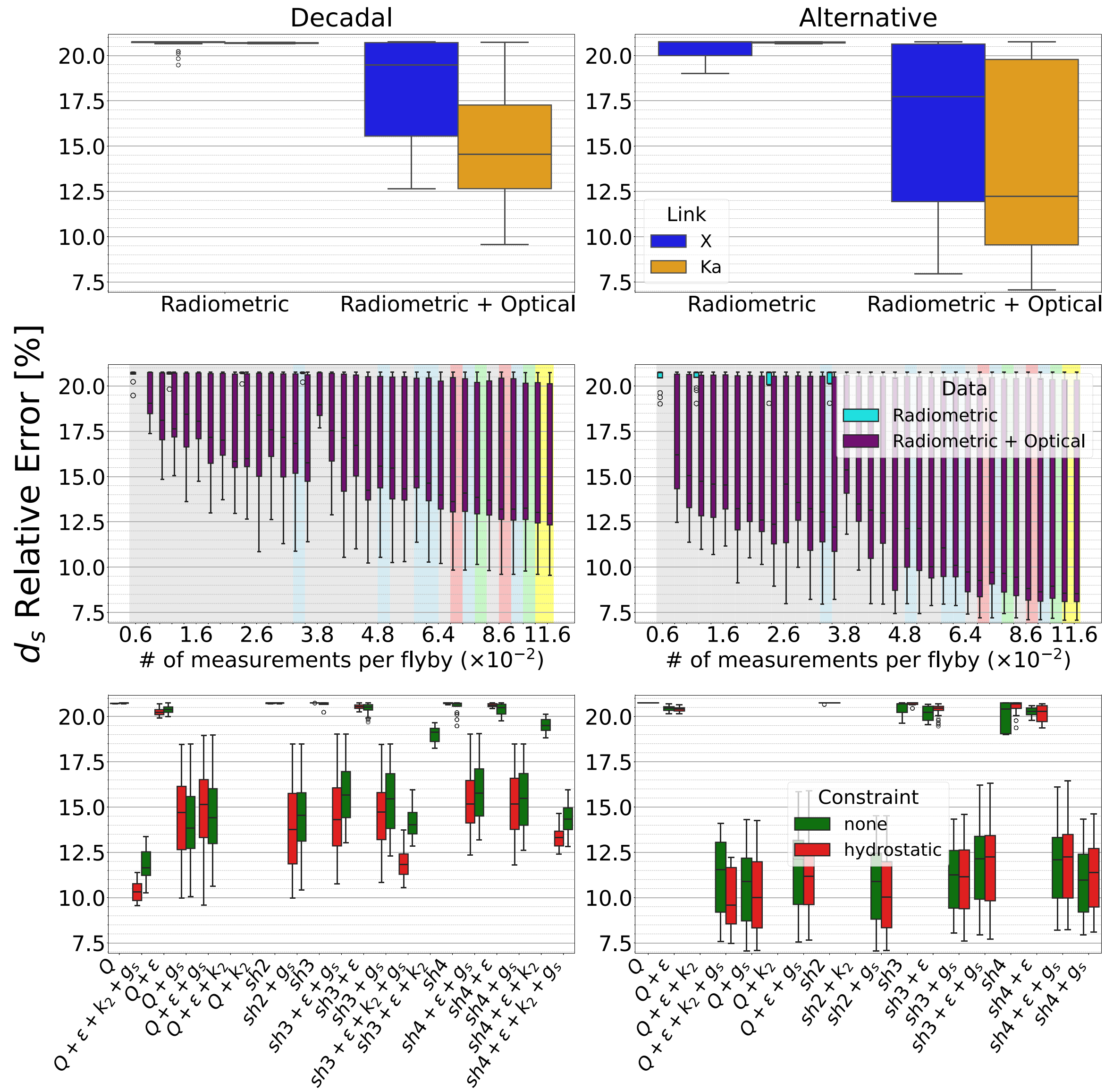

Figure 19. Interpolated uncertainty of Ariel's ice shell thickness (d_s). A detailed explanation of the figure can be found in Figure 10. The results of the sensitivity analysis for the remaining Uranian satellites are presented in a figure set in the online journal.

(The complete figure set (4 images) is available in the online article.)

The results of the aforementioned sensitivity analysis for the remaining Uranian satellites, namely Miranda, Umbriel, Titania, and Oberon, are provided in the form of a figure set in the online journal.

Appendix C
Lookup Tables

We provide the "lookup tables" that we have constructed in order to characterize the GS experiment for the future geophysical investigation of the Uranian moons. The tables are provided in machine-readable format, which can be filtered by satellite ("sat" column) and by interior model via the ocean thickness value ("ocean" column). A summary of the complete lookup tables, illustrating their structure and content, is provided in Table 8. The columns "sigma-moi," "sigma-k2," "sigma-lib," and "sigma-obl" represent the uncertainty scaling factor utilized to define the observables' uncertainty in the MCMC runs. This is calculated as, for instance, $\sigma_{\rm MoI} = {\rm MoI}^{*}$sigma-moi. Table 9 collects the interior truth values of the Uranian satellites, as well as the expected geodetic observables for each interior model. These can be employed to quantify the absolute uncertainty based on the provided uncertainty factors. Each line represents the output of a single MCMC run. The provided data set includes the 5th, 95th, 15.87th, and 84.13th percentile values of the a posteriori distributions of the investigated interior parameters, namely, ρ_c, ρ_o, d_o, ρ_s, and d_s. To illustrate, the column containing the 95th percentile value of ocean density (ρ_o) is designated as "95th-rho-o." As the rock-to-ice mass ratio (rock/ice) is determined directly from the interior parameter a posteriori distributions, the same percentiles are provided for this ratio, which is henceforth referred to as "ratio." For each interior parameter, including the rock-to-ice ratio, we also provide the ratio between the width of the 5th–95th percentile range and the width of the uniform prior distributions defined in Table 2 (also referred to as noninformative ratio). For example, for the ocean density ρ_o, it is "infRatio-rho-o."

Table 8
Machine-readable Format Example Table for Miranda

sat	sigma-moi	sigma-k2	sigma-lib	sigma-obl	ocean	5th-rho-c	95th-rho-c	5th-rho-o	95th-rho-o	5th-d-o	95th-d-o
Miranda	1	0.1	1	1	0	2653.9632	3468.6963	715.8306	1030.2059	576.4677	16698.1623
Miranda	1	1	1	1	0	2469.0415	3450.6254	717.9793	1033.1759	2147.5867	52578.6124
Miranda	1	0.1	0.1	1	0	2638.5007	3467.5551	715.7617	1029.9643	561.4932	16716.7990
Miranda	1	1	0.1	1	0	2479.5367	3453.6119	717.1165	1032.4058	1834.0822	44263.5632
Miranda	1	0.1	1	0.1	0	2647.1815	3467.5253	714.8648	1029.5303	543.0070	16049.1530

5th-rho-s	95th-rho-s	5th-d-s	95th-d-s	15th-rho-c	84th-rho-c	15th-rho-o	84th-rho-o	15th-d-o	84th-d-o	15th-rho-s	84th-rho-s
723.3713	1040.3274	89576.2042	135877.92	2836.8308	3399.1709	751.4338	988.6579	1853.1596	12501.4425	771.9491	1016.2167
728.8298	1040.3548	61573.9810	126873.75	2607.7915	3342.9144	755.1218	996.4336	6774.4329	41169.6717	785.3860	1016.9020
730.0151	1039.9144	89643.2431	136019.61	2823.0282	3395.5804	750.3411	988.2742	1802.1616	12431.2008	787.9383	1016.0347
729.9063	1037.3352	69386.0180	127515.51	2628.8227	3352.1752	754.2234	993.0543	5724.6623	34655.5708	785.5771	1010.2935
768.9488	1040.4720	94134.0552	136193.53	2832.7598	3395.3854	748.2802	986.1485	1751.7738	11949.5108	834.4036	1018.8537

15th-d-s	84th-d-s	5th-ratio	95th-ratio	15th-ratio	84th-ratio	infRatio-rho-c	infRatio-rho-o	infRatio-d-o	infRatio-rho-s	infRatio-d-s	infRatio-ratio
96535.1775	129063.0368	0.2109	0.9866	0.2548	0.8256	0.7407	0.8982	0.1612	0.9056	0.3858	0.2091
73233.8538	114451.3141	0.2285	0.9640	0.2802	0.7876	0.8923	0.9006	0.5043	0.8901	0.5442	0.1983
97323.1442	129407.1373	0.2115	0.9751	0.2539	0.7849	0.7537	0.8977	0.1616	0.8854	0.3865	0.2058
78839.6339	116208.5954	0.2323	0.9621	0.2867	0.7885	0.8855	0.9008	0.4243	0.8784	0.4844	0.1967
102611.1936	129989.9915	0.2103	0.8528	0.2493	0.6542	0.7458	0.8990	0.1551	0.7758	0.3505	0.1732

Note.

(This table is available in its entirety in machine-readable form in the online article.)

Table 9
Truth Interior Models with an Ocean

		Miranda	Ariel	Umbriel	Titania	Oberon
Three-layer Interiors						
Ice-I shell density	ρ_s (kg m^{-3})	950	950	950	950	950
Water ocean density	ρ_o (kg m^{-3})	1000	1000	1000	1000	1000
Rocky core density	ρ_c (kg m^{-3})	3060	3060	3060	3060	3060
Ice-I shell thickness	h_s (km)	114.55, 104.86, 95.21, 85.61, 76.07	190.70, 180.95, 171.22, 161.5, 151.8e	196.35, 186.61, 176.88, 167.16, 157.46	232.23, 222.48, 212.74, 203.01, 193.29	221.15, 211.4, 201.66, 191.93, 182.21
Water ocean thickness	(h_o km)	10,20,30,40,50	10,20,30,40,50	10,20,30,40,50	10,20,30,40,50	10,20,30,40,50
Rocky core radius	R_c (km)	111.25, 110.94, 110.59, 110.19, 109.73	378.2, 377.95, 377.68, 377.40, 377.1	378.35, 378.09, 377.82, 377.54, 377.24	546.67, 546.42, 546.16, 545.89, 545.61	530.25, 530., 529.74, 529.47, 529.19
MoI		0.341, 0.341, 0.3411, 0.3414, 0.3417	0.3123, 0.3123, 0.3123, 0.3124, 0.3125	0.3126, 0.3126, 0.3127, 0.3127, 0.3128	0.3116, 0.3117, 0.3117, 0.3117, 0.3117	0.3117, 0.3117, 0.3117, 0.3118, 0.3118
k_2		0.00128, 0.00148, 0.00174, 0.00208, 0.00252	0.01441, 0.01563, 0.017, 0.01854, 0.02028	0.01425, 0.01543, 0.01675, 0.01824, 0.0199	0.03089, 0.03285, 0.03499, 0.03732, 0.03987	0.02945, 0.03141, 0.03356, 0.03591, 0.03850
g_s	10^{-6} rad	−218.12, −222.52, −228.74, −237.46, −249.68	−45.42, −46.44, −47.61, −48.98, −50.57	−53.92, −55.05, −56.35, −57.85, −59.59	−3.69, −3.76, −3.85, −3.94, −4.04	−1.75, −1.79, −1.83, −1.88, −1.94
ε	10^{-6} rad	354.83, 355.07, 355., 354.81, 354.48	15.78, 12.75, 12.86, 12.91, 12.94	11.11, 27.74, 22.25, 22.27, 22.32	225.87, 206.32, 355.29, 245.87, 332.97	2331.36, 5687.76, 1339.95, 1376.76, 1336.43

ORCID iDs

Valerio Filice https://orcid.org/0000-0001-8009-1018
Gael Cascioli https://orcid.org/0000-0001-9070-7947
Sébastien Le Maistre https://orcid.org/0000-0002-9524-9479
Rose-Marie Baland https://orcid.org/0000-0002-5907-0033
Antony Trinh https://orcid.org/0000-0001-6732-4104
Erwan Mazarico https://orcid.org/0000-0003-3456-427X
Sander Goossens https://orcid.org/0000-0002-7707-1128

References

Archinal, B. A., Acton, C. H., A'Hearn, M. F., et al. 2018, CeMDA, 130, 22
Asmar, S. W., Armstrong, J. W., Iess, L., & Tortora, P. 2005, RaSc, 40, RS2001
Asmar, S. W., Bolton, S. J., Buccino, D. R., et al. 2017, SSRv, 213, 205
Baland, R.-M., Coyette, A., & Van Hoolst, T. 2019, CeMDA, 131, 11
Baland, R.-M., Filice, V., Le Maistre, S., et al. 2025, Icar, 426, 116371
Baland, R.-M., & Van Hoolst, T. 2010, Icar, 209, 651
Baland, R. M., van Hoolst, T., Yseboodt, M., & Karatekin, Ö. 2011, A&A, 530, A141
Bernauer, F., Garcia, R. F., Murdoch, N., et al. 2020, EP&S, 72, 191
Bertone, S., Mazarico, E., Barker, M. K., et al. 2021, JGRE, 126, e2020JE006683
Bertotti, B., Comoretto, G., & Iess, L. 1993, A&A, 269, 608
Bierson, C. J., & Nimmo, F. 2022, Icar, 373, 114776
Bills, B. G., & Nimmo, F. 2009, LPSC, 40, 1462
Bindschadler, D., Hwangpo, N., & Sarrel, M. 2022, in 2022 IEEE Aerospace Conf. (AERO), 1
Buccino, D. R., Kahan, D. S., Parisi, M., et al. 2021, RaSc, 56, e07387
Burmeister, S., Willner, K., Schmidt, V., & Oberst, J. 2018, JGeod, 92, 963
Cappuccio, P., Hickey, A., Durante, D., et al. 2020, P&SS, 187, 104902
Cartwright, R., Emery, J., Rivkin, A., Trilling, D., & Pinilla-Alonso, N. 2015, Icar, 257, 428
Cascioli, G., Mazarico, E., Dombard, A. J., & Nimmo, F. 2024, PSJ, 5, 45
Castillo-Rogez, J., Weiss, B., Beddingfield, C., et al. 2023, JGRE, 128, e2022JE007432
Durante, D., Hemingway, D., Racioppa, P., Iess, L., & Stevenson, D. 2019, Icar, 326, 123
Eanes, R., Schutz, B., & Tapley, B. 1983, in Proc. 9th Int. Symp. Earth Tides, ed. J. T. Kuo (Stuttgart: Schweizerbart Science Publishers), 239
Ermakov, A. I., Park, R. S., Roa, J., et al. 2021, PSJ, 2, 157
Evans, S., Taber, W., Drain, T., et al. 2018, CEAS, 10, 79
Filice, V., Le Maistre, S., Dehant, V., et al. 2024, EP&S, 76, 12
Foreman-Mackey, D., Hogg, D. W., Lang, D., & Goodman, J. 2013, PASP, 125, 306
Genova, A., Goossens, S., Mazarico, E., et al. 2019, GeoRL, 46, 3625
Genova, A., Parisi, M., Gargiulo, A. M., et al. 2024, PSJ, 5, 40
Goossens, S., van Noort, B., Mateo, A., Mazarico, E., & van der Wal, W. 2024, NatAs, 8, 846
Hussmann, H., Sohl, F., & Spohn, T. 2006, Icar, 185, 258
Iess, L., Jacobson, R. A., Ducci, M., et al. 2012, Sci, 337, 457
Iess, L., Stevenson, D. J., Parisi, M., et al. 2014, Sci, 344, 78
Jacobson, R. A. 2014, AJ, 148, 76
Kaula, W. M. 1966, Theory of Satellite Geodesy. Applications of Satellites to Geodesy (Waltham, MA: Blaisdell)
Konopliv, A. S., Asmar, S. W., Park, R. S., et al. 2014, Icar, 240, 103
Lainey, V., Rambaux, N., Tobie, G., et al. 2024, Natur, 626, 280
Love, A. E. H. 1911, Some Problems of Geodynamics (Cambridge: Cambridge Univ. Press)
Margot, J.-L., Peale, S. J., Solomon, S. C., et al. 2012, JGRE, 117, E00L09
Matsuyama, I., Nimmo, F., Keane, J. T., et al. 2016, GeoRL, 43, 8365
Mazarico, E., Buccino, D., Castillo-Rogez, J., et al. 2023, SSRv, 219, 30
McCarthy, D. D., & Petit, G. 2004, IERS Conventions (2003) Technical Note 32, IERS
Meriggiola, R., Iess, L., Stiles, B. W., Lunine, J. I., & Mitri, G. 2016, Icar, 275, 183
Milani, A., & Gronchi, G. 2009, Theory of Orbit Determination (Cambridge: Cambridge Univ. Press)
Nadezhdina, I. E., Zubarev, A. E., Brusnikin, E. S., & Oberst, J. 2016, ISPAr, 41, 459
National Academies of Sciences 2023, Origins, Worlds, and Life: A Decadal Strategy for Planetary Science and Astrobiology 2023-2032 (Washington, DC: The National Academies Press)
Noble, M. W., Conard, S. J., Weaver, H. A., Hayes, J. R., & Cheng, A. F. 2009, Proc. SPIE, 7441, 74410Y
Pappalardo, R. T., Buratti, B. J., Korth, H., et al. 2024, SSRv, 220, 40
Park, R. S., Asmar, S. W., Buffington, B. B., et al. 2011, GeoRL, 38, L24202
Park, R. S., Mastrodemos, N., Jacobson, R. A., et al. 2024, JGRE, 129, e2023JE008054
Park, R. S., Riedel, J. E., Ermakov, A. I., et al. 2020, P&SS, 194, 105095
Petricca, F., Genova, A., Castillo-Rogez, J. C., et al. 2023, GeoRL, 50, e2023GL104016
Robert, C. P., & Casella, G. 2004, Monte Carlo Statistical Methods (New York: Springer)
Sabadini, R., Vermeersen, B., & Cambiotti, G. 2016, Global Dynamics of the Earth: Applications of Viscoelastic Relaxation Theory to Solid-Earth and Planetary Geophysics (Dordrecht: Springer)
Simon, A., Nimmo, F., & Anderson, R. 2021, Uranus Orbiter and Probe: Journey to an Ice Giants System, National Aeronautics and Space Administration
Smith, B. A., Soderblom, L. A., Beebe, R., et al. 1986, Sci, 233, 43
Stiles, B. W., Kirk, R. L., Lorenz, R. D., et al. 2008, AJ, 135, 1669
Tajeddine, R., Rambaux, N., Lainey, V., et al. 2014, Sci, 346, 322
Tapley, B. D., Schutz, B. E., & Born, G. H. 2004, Statistical Orbit Determination (Amsterdam: Elsevier)
Thomas, P., Tajeddine, R., Tiscareno, M., et al. 2016, Icar, 264, 37
Thomas, P. C. 1988, Icar, 73, 427
Tyler, G. L., Sweetnam, D. N., Anderson, J. D., et al. 1986, Sci, 233, 79
Van Hoolst, T., Baland, R.-M., & Trinh, A. 2013, Icar, 226, 299
Van Hoolst, T., Baland, R.-M., & Trinh, A. 2016, Icar, 277, 311
Van Hoolst, T., Rambaux, N., Karatekin, Ö., Dehant, V., & Rivoldini, A. 2008, Icar, 195, 386
Wahr, J. M., Zuber, M. T., Smith, D. E., & Lunine, J. I. 2006, JGRE, 111, E12005